HIGHWAY RESEARCH
RECORD

Number 108

Mechanics in Earth Masses
7 Reports

Presented at the
44th ANNUAL MEETING
January 11-15, 1965

SUBJECT CLASSIFICATION

63 Mechanics (Earth Mass)

25 Pavement Design

Department of Soils, Geology and Foundations
Eldon J. Yoder, Chairman
Joint Highway Research Project
Purdue University, Lafayette, Indiana

DIVISION B

H. Bolton Seed, Chairman
Department of Civil Engineering
University of California, Berkeley

COMMITTEE ON MECHANICS OF EARTH MASSES AND LAYERED SYSTEMS
(As of December 31, 1964)
Robert L. Schiffman, Chairman
Professor of Soil Mechanics
Rensselaer Polytechnic Institute, Troy, New York

Richard G. Ahlvin, Chief Engineer, Special Projects Section, Waterways Experiment Station, Vicksburg, Mississippi

Donald M. Burmister, Columbia University, New York, New York

Lawrence A. DuBose, Testing Service Corporation, Wheaton, Illinois

Jacob Feld, Consulting Engineer, New York, New York

Delon Hampton, Civil Engineering Department, School of Engineering and Applied Sciences, Kansas State University, Manhattan

Milton E. Harr, Associate Professor of Soil Mechanics, School of Civil Engineering, Purdue University, Lafayette, Indiana

R. L. Kondner, Department of Civil Engineering, Northwestern University, Evanston, Illinois

Charles C. Ladd, Assistant Professor of Civil Engineering, Massachusetts Institute of Technology, Cambridge

T. F. McMahon, U. S. Bureau of Public Roads, Washington, D. C.

Robert L. McNeill, Supervisor, Soil Dynamics, Shock Tube Laboratory, Albuquerque, New Mexico

Z. C. Moh, Department of Engineering and Applied Science, Yale University, New Haven, Connecticut

F. E. Richart, Jr., University of Michigan, Ann Arbor

B. B. Schimming, Department of Civil Engineering, Notre Dame University, Notre Dame, Indiana

Werner E. Schmid, Department of Civil Engineering, Princeton University, Princeton, New Jersey

F. H. Scrivner, Research Engineer, Texas Transportation Institute, Texas A & M University, College Station

Eugene L. Skok, Jr., Department of Civil Engineering, University of Minnesota, Minneapolis

A. A. Vesic, Department of Civil Engineering, Georgia Institute of Technology, Atlanta

H. E. Wahls, Department of Civil Engineering, North Carolina State University, Raleigh

William G. Weber, Jr., Senior Materials and Research Engineer, California Division of Highways, Sacramento

Foreword

This Record is devoted to the subject of measurement and computation of load-deformation relationships in earth masses. The seven papers presented here range from the reporting of results of full-scale tests to development of theoretical relationships permitting computation of the values involved.

Baker and Kondner report on pullout load capacity tests on small-scale earth anchors and present data on computed pullout capacities for various size anchors embedded at different depths, as well as data on full-scale field tests on earth anchors.

Authors Barksdale and Harr present an influence chart for computing the vertical stress increase in the interior of a semi-infinite homogeneous, isotropic, elastic mass due to distributed horizontal shearing stresses applied at the surface. The authors also give an example illustrating the use the chart.

Moore shows that the apparent elastic modulus and the apparent Poisson's ratio are not the same as the true elastic constants appearing in Hooke's law. By assuming that the soil behaves elastically, Moore shows that the true elastic constants (Young's modulus and Poisson's ratio) can be determined by applying corrections to the apparent values obtained in triaxial testing.

In their paper Schimming and Valera employ the Voigt model and two-dimensional viscoelastic displacement equations applicable to the model to determine, on a numerical basis, the effect of viscosity on the load-settlement-time relation in an ideal soil. They also present charts indicating the viscosity effect on surface settlement and displacement within the soil mass as a function of time for an applied load.

Kondner and Pfister have extended their studies (previously reported to the Highway Research Board) on the lateral stability of rigid poles in dry sand by considering the effect of void ratio on lateral stability of rigid poles embedded in saturated sand. Void ratio effects are expressed in the dimensionless parameter of relative density. Equations are given which take into account the size of the pole, the depth of embedment, and the relative density of the sand.

Goodman, Hegedus and Haley report on studies of resistance to penetration of small-scale footings when tested at constant rates of penetration (sinkage) ranging from 0.2 to 1,750 in./min. Tests were made in Ottawa sand and in Boston blue clay. Goodman and Liston in their paper on land locomotion mechanics show that motion resistance to movement of vehicles on land is proportional to sinkage and the tractive effort is proportional to the shear strength. They develop equations showing the interrelationships.

Contents

Pullout Load Capacity of a Circular Earth Anchor Buried in Sand

WALLACE H. BAKER and ROBERT L. KONDNER
Respectively, Graduate Student and Associate Professor of Civil Engineering,
Northwestern University

The results of pullout load capacity tests performed on numerous small-scale model earth anchors are presented. The techniques of dimensional analysis are used to develop empirical relationships among anchor size, depth of anchor embedment, and pullout capacity for single anchors of circular cross-section buried in a dense uniform sand. A distinction is made between shallow and deep anchors. The range of the ratio of depth of embedment to anchor diameter studied corresponds to the general range found in field applications of earth anchors that are used to provide tieback resistance for retaining structures and uplift resistance for transmission towers, utility poles, moorings, etc. The results of two full-scale field tests of Webb-Lipow type anchors are also reported.

•THIS INVESTIGATION presents the results of pullout load capacity tests performed on numerous small-scale model earth anchors. The range of the ratio of depth of embedment to anchor diameter (h/d) studied corresponds to the general range found in field applications of earth anchors.

The purpose of the investigation was to develop an empirical relationship among the depth of anchor embedment, anchor width, and pullout capacity of earth anchors, and to define the transition point from a shallow failure to a deep failure for increasing depth of embedment. The study was limited to tests performed on single anchors of circular cross-sectional shape buried in a dense uniform sand. The results of pull-out load capacity tests performed on two full-scale field earth anchors of the Webb-Lipow type are also reported.

Earth anchors are used to provide uplift resistance for transmission towers (1, 2), utility poles, aircraft moorings, submerged pipelines (3) and tunnels (4), and to develop the tieback forces required to eliminate external bracing from retaining structures and sheeting walls (5, 6, 7, 8). The use of earth anchors in specific projects has been limited by a number of factors including the lack of economical methods of in-place construction, the absence of a rational approach to the design of earth anchor systems (9), and the general unfamiliarity of the industry with the possible uses of earth anchors.

Although several types of prefabricated earth anchors are commercially available, they cause serious disturbance to the surrounding soil during installation. The effect of such soil disturbance may be a major reduction in the pullout capacity of the anchor. To take full advantage of the natural strength of the soil, an anchor should be constructed in place without disturbing the soil. Anchors can be constructed in place in the following manner: first, a small-diameter shaft is drilled to the necessary depth; next, an expandable reaming device is used to enlarge the bottom of the shaft hole to the desired diameter; and finally, the enlarged hole is filled with concrete and reinforcing steel to form the required anchorage (7).
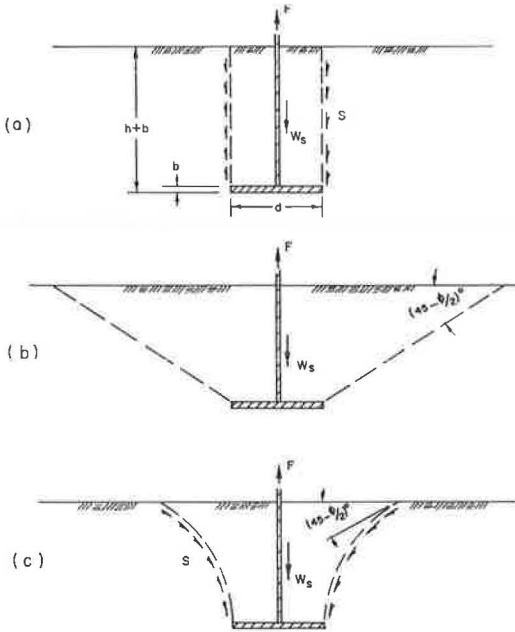
Figure 1. Methods for calculating pullout load capacity for earth anchors: (a) friction cylinder method, (b) soil cone method, and (c) Ball's method.

Present methods for calculating the pullout capacity of anchors in sand are based on an assumed shape for the failure surface and, with the exception of Balla's (10) method, give results contrary to those observed.

The friction cylinder method (earth pressure method, Swiss formula, Frohlich-Majer's procedure, 10) assumes that failure occurs along the surface of a cylinder of soil above the anchor. The cylinder has the same cross-section as the horizontal projection of the anchor (Fig. 1a). The pullout capacity is computed by considering the weight of the cylinder of soil and the frictional resistance along its surface.

The weight-of-cone method (earth load method, Mohr's formula, 10) assumes that the failure surface takes the shape of a truncated cone extending above the anchor with an apex angle of $90 + \phi$ (Fig. 1b). The pullout capacity is given as the weight of the soil within the truncated cone.

The method presented by Balla (10) is based on the shape of the failure surface observed during small-scale model anchor tests (Fig. 1c) in sand. Applying Kötter's equation to this failure surface, he computed the theoretical pullout capacity for circular anchors and showed it to be proportional to the third power of the depth of embedment. Such a theoretical analysis gives adequate correlation with Balla's small-scale model anchor tests, the model tests conducted in this study for a h/d ratio less than 6, several field tests of shallow anchors reported by Balla, and the shallow field test reported herein. According to the results of the present study, however, when extended to a h/d ratio greater than 6, Balla's method gives a pullout capacity greater than that actually developed. Thus, his method should not be considered applicable to deep anchors.

DIMENSIONAL ANALYSIS

Dimensional analysis, formalized by Buckingham (11) in his well-known π-theorem, has been used by numerous researchers to determine the functional relationships between the primary physical constants involved in physical phenomena. In this respect, dimensional analysis is often helpful in providing a simple basis for the possible correlation of the results of small-scale model tests with the behavior of full-scale prototypes.

According to the π-theorem, a physical phenomenon which is a function of n physical quantities involving m fundamental units can be described in the following functional form:

$$F\left(\pi_1, \pi_2, \ldots, \pi_{n-m}\right) = 0 \qquad (1)$$

where the π-terms are the (n - m) independent dimensionless products of the n physical quantities (6).

The primary physical quantities for the pullout capacity of a flat anchor buried in sand are listed in Table 1 using the force, length, and time system of fundamental units.

TABLE 1

PRIMARY PHYSICAL QUANTITIES USED IN DIMEN-
SIONAL ANALYSIS OF A FLAT CIRCULAR ANCHOR
EMBEDDED IN SAND

Physical Quantity	Symbol	Fundamental Units
Pullout load capacity	F	F
Cross-sectional area of anchor	A	L^2
Perimeter of anchor	c	L
Thickness of anchor	b	L
Depth of embedment	h	L
Unit weight of soil	γ	FL^{-3}
Angle of internal friction	ϕ	$F^\circ L^\circ T^\circ$
Relative density	D_d	$F^\circ L^\circ T^\circ$
Void ratio	e	$F^\circ L^\circ T^\circ$
Time of loading	t	T
Rate of loading	r	FT^{-1}

By appropriate manipulations, the eleven physical quantities yield the following eight π-terms: $\pi_1 = F/ha\gamma$, $\pi_2 = h^2/A$, $\pi_3 = c/b$, $\pi_4 = \gamma hA/rt$, $\pi_5 = c^2A$, $\pi_6 = \phi$, $\pi_7 = D_d$, and $\pi_8 = e$. For this set of π-terms, Eq. 1 implies the functional relation:

$$F/ha\gamma = f_1\left(h^2/A, \ c/b, \ \gamma hA/rt, \ c^2/A, \ \phi, \ D_d, \ e\right) \quad (2)$$

By additional algebraic transformations, an alternate set of independent π-terms can be obtained which yields the functional relation:

$$F/c^3\gamma = f_2\left(h/c, \ c/b, \ \gamma hA/rt, \ c^2/A, \ \phi, \ D_d, \ e\right) \quad (3)$$

For anchors of circular cross-section, with diameter d, the following simplification of π-terms is possible: $F/hA\gamma \rightarrow F/hd^2\gamma$, $F/c^3\gamma \rightarrow F/d^3\gamma$, $\gamma hA/rt \rightarrow \gamma hd^2/rt$, $c^2/A \rightarrow 4\pi$.

By varying the rate of loading, the dimensionless parameter $\gamma hd^2/rt$ can be kept relatively constant and, hence, its effects can be minimized. The flow characteristics or viscosity of the sand is assumed to be a function of the soil properties γ, ϕ, D_d, and e and, therefore, is not considered an independent variable.

If all tests are conducted in the same sand at a constant density, the parameters ϕ, D_d, and e can be considered constants. Subject to the preceding restrictions, Eqs. 2 and 3 reduce to:

$$F/hd^2\gamma = g_1 (h^2/d^2, \ d/b) \quad (4)$$

and

$$F/d^3\gamma = g_2 (h/d, \ d/b) \quad (5)$$

respectively. The explicit forms of Eqs. 4 and 5 must be determined by experiment.

EXPERIMENTAL PROCEDURE

The model anchors for this study were flat circular $\frac{1}{4}$-in. thick steel plates with diameters of 1.00, 1.50, 2.00, and 3.00 in. An 0.078-in. diameter straight piano wire was inserted in the center of each anchor to serve as a tie rod. The model tests were conducted at depths of embedment of 3.0, 6.0, 9.0, 12.0, 15.0, 18.0, and 21.0 in.

A schematic drawing of the loading system is shown in Figure 2. Vertical load was applied to the anchor in increments through a cable and pulley system with a swivel joint inserted between the tie rod connection and the cable to allow the cable to twist. Movement of the anchor was measured by a reverse-reading deflection dial mounted on a reference beam.

The model anchor tests were conducted in an air-dry uniform silica sand (ASTM 20-30 Ottawa sand) with the following properties: specific gravity, G = 2.66; angle of internal friction, ϕ = 42 deg; average unit weight, $\gamma_{avg.}$ = 112.1 pcf. The unit weight ranged from 111.8 to 112.5 pcf for all tests.

The sand was placed in a metal tank through a No. 12 U.S. standard sieve held 20 to 30 in. above the surface of the sand. The sieve was moved slowly back and forth across the tank in a rectangular grid pattern. When the sand was at the desired depth below the top of the tank, the anchor was carefully set in place, and the sieving operation continued to the top of the tank. The sand was weighed after the test to compute the average unit weight.
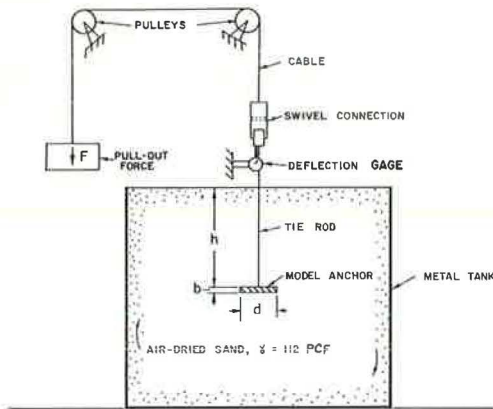
Figure 2.   Test setup and loading apparatus for model anchor tests.

To study the shape of the failure surface developed for shallow and deep anchors, supplemental anchor tests were conducted in a clear plexiglass tank containing colored sand strata. The tank was made of $\frac{1}{2}$-in. plexiglass screwed and glued together to form an open-top box 35 by 7 in. in plan and 22 by 35 in. in profile. The anchors used were flat steel plates measuring 7.0 by 1.0, 2.0, and 3.0 in., respectively.

The colored sand layers for the tests were made by placing a thin layer of black (dyed) ASTM 20-30 Ottawa sand against the front wall of the tank at 1-in. vertical intervals. Loads were applied until a failure surface developed or until the anchor was pulled out the tank.

EXPERIMENTAL RESULTS

The experimental data for the model anchor tests conducted in this study are given in Table 2. The average value of pullout capacity vs depth is plotted for each anchor diameter in Figure 3.

The pullout capacity was defined as the smallest load causing a disproportionate movement of the anchor. For the majority of tests, the pullout capacity was the maximum load resistance attained by the anchor. However, for a few tests the first large movement of the anchor was followed by a small increase in load resistance. For the few cases having this type of load-deflection response, the h/d's were all equal to or greater than 6. A typical example of this type of load-deflection response is shown in Figure 4.

For shallow anchors (h/d < 6), a definite failure circle was observed to develop on the surface of the sand as the anchor system failed (Fig. 5a). For deep anchors (h/d ≥ 6), however, only a sight rise in the surface of the sand occurred in the vicinity of the tie rod at failure.

The 3-in. wide anchor tested at a depth of 14-in. in the plexiglass tank developed a definite failure surface (Fig. 5b) similar in shape to that proposed by Balla (10). The 1- and 2-in. wide anchors tested at the same depth in the plexiglass tank did not produce a visible failure surface until the anchor had been pulled to within a few inches of the surface and was acting as a "shallow" anchor.

TABLE 2

EXPERIMENTAL DATA—MODEL TESTS

| Test No.	Depth, h (in.)	Diameter, d (in.)	Pullout Capacity, F (lb)	Radius of Failure Circle (in.)	Unit Weight, γ_t (pcf)
1	3	1.0	2.2	2.15	—
2	3	1.0	2.2	2.30	112.09
3	6	1.0	12.6	—	—
4	6	1.0	11.0	—	111.96
5	9	1.0	32.9	—	111.91
6	12	1.0	52.9	—	—
7	12	1.0	55.6	—	112.30
8	15	1.0	81.6	—	112.44
9	18	1.0	110.2	—	111.93
10	18	1.0	79.4	—	112.47
11	21	1.0	130.1	—	111.76
12	9	1.5	35.7	—	112.33
13	12	1.5	66.1	—	112.27
14	12	1.5	72.8	—	—
15	15	1.5	105.8	—	111.93
16	18	1.5	141.1	—	112.33
17	3	2.0	3.5	2.45	—
18	6	2.0	15.4	4.20	—
19	6	2.0	15.4	4.00	—
20	9	2.0	39.7	—	112.04
21	12	2.0	79.4	—	—
22	15	2.0	138.9	—	111.82
23	15	2.0	138.9	—	112.19
24	18	2.0	200.7	—	—
25	21	2.0	247.0	—	111.99
26	21	2.0	211.7	—	—
27	3	3.0	5.5	4.35	—
28	6	3.0	17.9	4.60	—
29	9	3.0	49.6	6.25	112.04
30	9	3.0	49.0	6.60	—
31	12	3.0	95.3	8.00	111.93
32	15	3.0	167.6	—	111.82
33	18	3.0	273.4	—	111.88
34	18	3.0	264.6	—	112.19
35	21	3.0	388.1	—	111.79
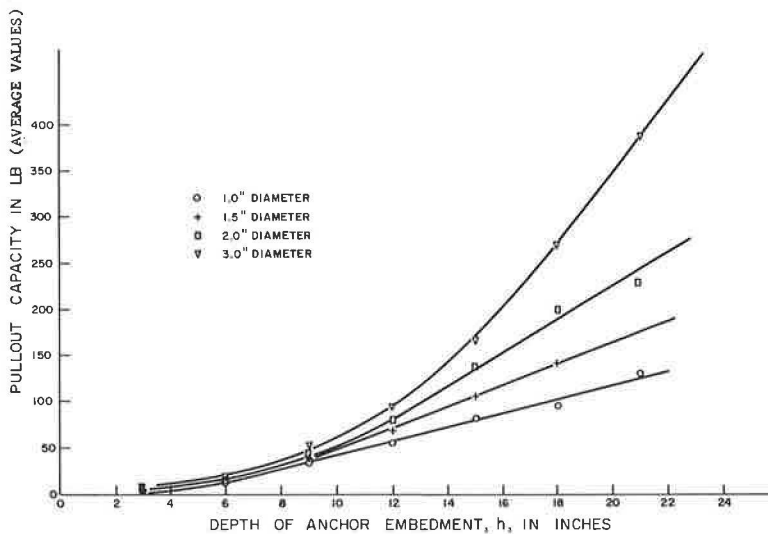
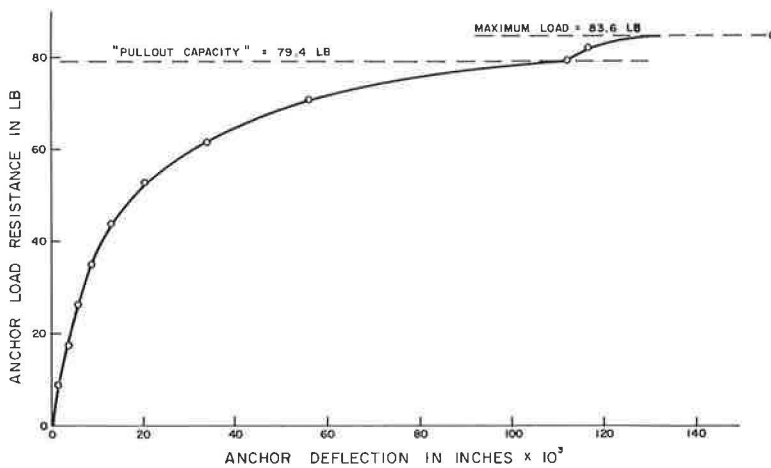Figure 3. Plot of anchor pullout capacity vs depth of anchor embedment.

Figure 4. Load vs deflection curve for model test No. 21.

Figure 5. (a) failure circle developed by shallow anchor (h/d < 6); and (b) shape of two-dimensional failure surface developed by 3-in. wide anchor.

DISCUSSION OF RESULTS

The appearance of a failure circle on the sand surface only for shallow anchors (h/d < 6) indicates a difference in the mode of failure between deep and shallow anchors. This difference would logically be represented by two distinct functional equations relating the primary quantities.

The test results shown in Figure 3 are plotted in Figure 6 in terms of the dimensionless parameters $F/hd^2\gamma$ and h^2/d^2. For the range h/d < 6, the curve in Figure 6 appears to be insensitive to changes in the parameter d/b. This portion of Figure 6 is plotted in Figure 7 and can be approximated by a straight line. Thus Eq. 4 has the form, for h/d < 6:
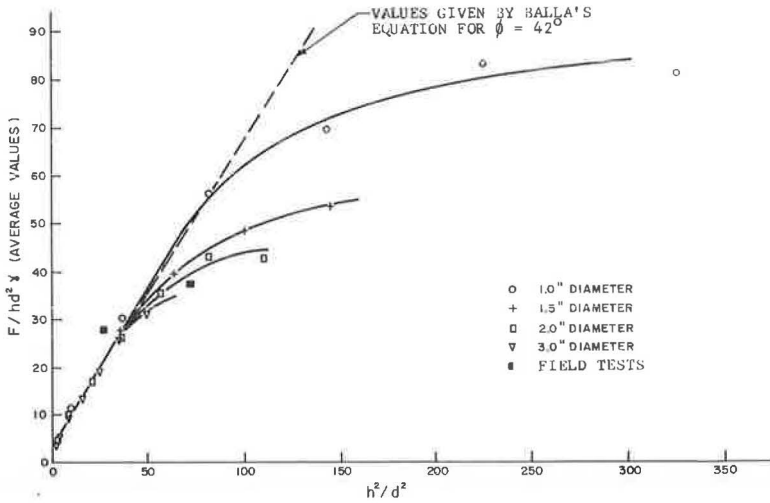
Figure 6. Plot of $F/hd^2\gamma$ vs h^2/d^2.
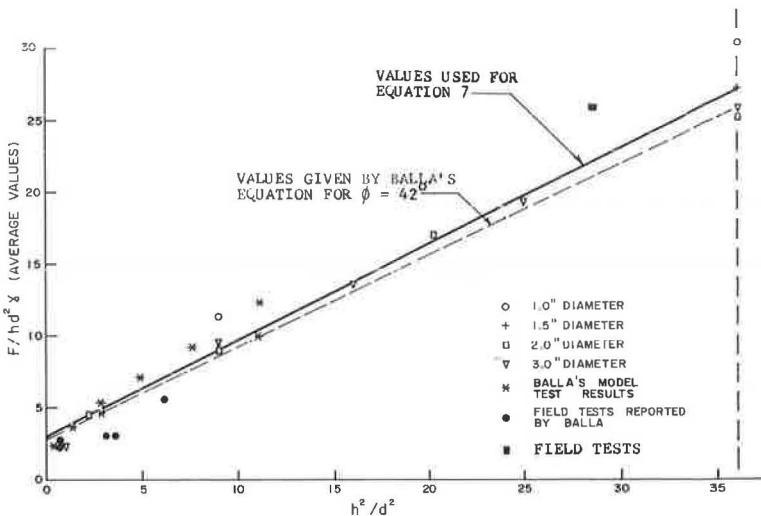
Figure 7. Plot of $F/hd^2\gamma$ vs h^2/d^2 for h/d $\leq$ 6.

$$F/hd^2\gamma \;=\; C_1 \;+\; C_2 h^2/d^2 \tag{6}$$

where C_1 is the intercept and C_2 is the slope of the straight-line portion of the curve in Figure 7. Solving for the pullout capacity yields, for $h/d < 6$:

$$F \;=\; C_1 hd^2\gamma \;+\; C_2 h^3\gamma \tag{7}$$

where $C_1 = 3.0$ and $C_2 = 0.67$ for the particular values of ϕ, D_d, and e used. The constants C_1 and C_2 are presumably functions of ϕ and D_d. Such an assumption allows Eq. 7 to be written in the form
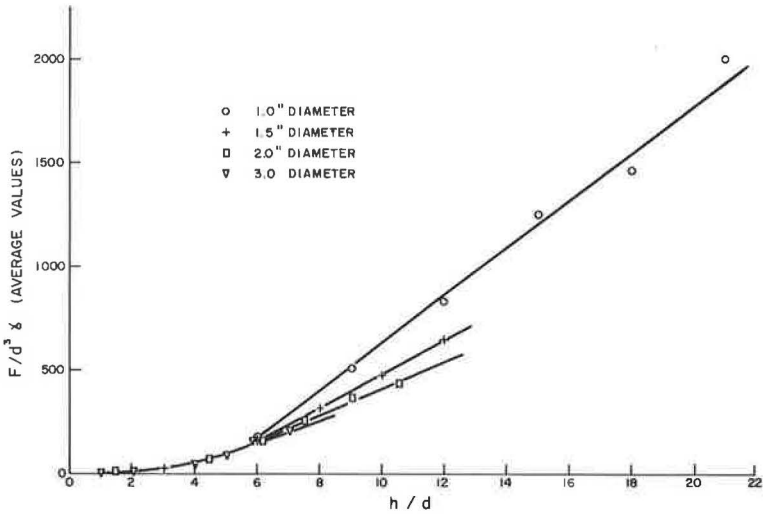
Figure 8. Plot of $F/d^3\gamma$ vs h/d.
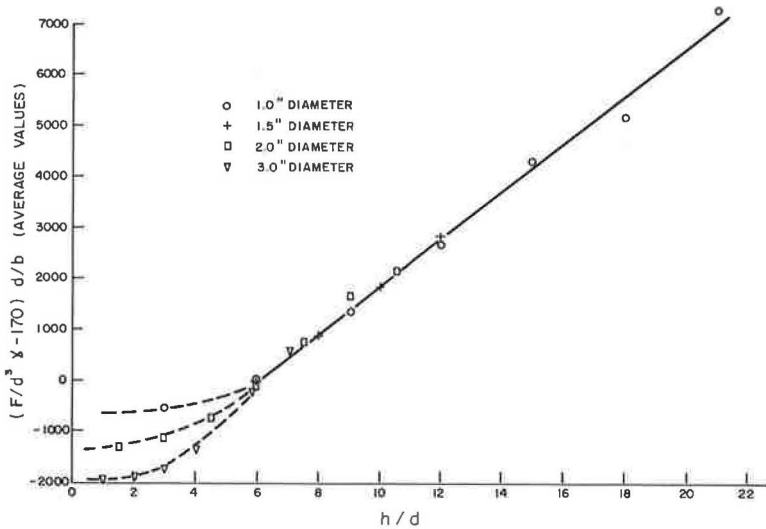
Figure 9. Plot of parameters $(F/d^3\gamma - 170)$ d/b vs h/d.

$$F = h^3\gamma\left[H_1\left(\phi, D_d\right) + H_2\left(\phi, D_d\right)\left(d^2/h^2\right)\right] \qquad (8)$$

for $h/d < 6$. Eq. 8 is similar in form to Balla's equation for circular anchors in cohesionless soil (10) which can be written:

$$F = h^3\gamma\left[H_1\left(\phi, h/d\right) + H_2\left(\phi, h/d\right)\right] \qquad (9)$$

Balla's results have been plotted in Figure 7 in dimensionless form. Use of Eqs. 8 or 9 gives pullout capacities larger than those actually observed in the model tests for $h/d > 6$, as shown in Figure 6.

Because the thickness, b, of the anchor does not appear in either Eq. 7 or Balla's equation, these equations do not apply to anchors with small values of d/b (e.g., $d/d < 1$) since such anchors act primarily as friction piles.

The test results are plotted in terms of the alternate dimensionless parameters $F/d^3\gamma$ and h/d in Figure 8. The parameter $F/d^3\gamma$ is a function of d/b for $h/d > 6$ and converges to $F/d^3\gamma = 170$ for $h/d = 6$.

If the origin in Figure 8 is moved upwards to $F/d^3\gamma = 170$ and the ordinate is then multiplied by d/b, the several curves shown for $h/d > 6$ in Figure 8 reduce to the single curve shown in Figure 9. For the range $h/d \geq 6$, the curve in Figure 9 can be approximated by a straight line. Thus, Eq. 5 has the modified form, for $h/d \geq 6$:

$$\left(F/d^3\gamma - 170\right)d/b = C_3 + C_4 h/d \qquad (10)$$

where C_3 is the intercept and C_4 is the slope of the curve in Figure 9. Solving Eq. 10 for the pullout capacity yields, for $h/d \geq 6$:

$$F = 170\,d^3\gamma + C_3 d^2 b\gamma + C_4 h d b\gamma \qquad (11)$$

where $C_3 = 2,800$ and $C_4 = 470$ for the particular values of ϕ, D_d, and e used.

Because of the limited range of d/b values included in this study, it was not possible to determine whether Eq. 11 is applicable to anchors with values of $d/b < 4$.

The equations presented herein for the pullout capacity of a circular anchor buried in sand are based entirely on the results of small-scale model tests conducted in a specific sand having particular properties. For Eqs. 7 and 11 to be useful in actual design, empirical values for C_1, C_2, C_3, and C_4 must be determined for various values of ϕ and D_d, and must also be correlated with the results of full-scale field tests. The correlation between model and field tests is especially important since the size of the sand grains used in the laboratory cannot be reduced to the same scale as the model anchor. Such a contradiction in the geometrical similitude between the model and the prototype may produce unexpected effects.

FIELD TESTS

Pullout load capacity tests were performed on two full-scale field earth anchors of the Webb-Lipow type buried in a relatively uniform fine sand (dune deposits) at the site of the Redondo Steam Station of the Southern California Edison Co., Los Angeles, Calif. Average soil properties were as follows (13): angle of internal friction, $\phi = 37$ deg; dry unit weight, $\gamma_{dry} = 105$ pcf and in-place unit weight, $\gamma_t = 112$ pcf. Groundwater was encountered at a depth of about 18 ft below the surface.

The anchors were installed and tested by Webb and Lipow, General Engineering Contractors, Los Angeles, Calif. A 5-in. diameter shaft was first drilled and cased to about the desired anchor depth. AM-9 chemical grout was then placed at the bottom of the shaft to stabilize the sand during the subsequent reaming operation. A relatively weak grout was used so that the strength characteristics of the sand would not be significantly changed. Next, an expandable reaming tool fitted to a rotary vacuum drill rig was used to produce a cone-shaped void at the bottom of the shaft. The anchor was formed by filling the void with concrete after a $7/8$-in. diameter high-strength steel tie
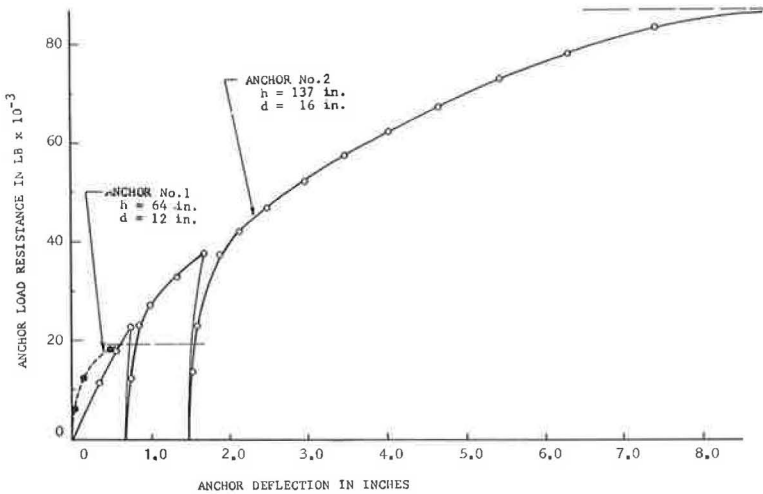
Figure 10. Plot of load vs deflection for field tests.
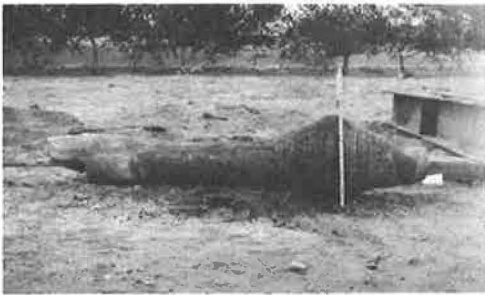
Figure 11. Field anchor No. 2 after testing.

rod had been inserted in the shaft. A special reinforcing device was used at the end of the tie rod to develop bond between the rod and the concrete.

Load was applied to the earth anchors in increments with a calibrated center-hole hydraulic jack supported by two steel reaction beams. Movement of the anchor was measured by a tensioned reference wire read against a scale fastened to the tie rod. Results of the two field tests and the dimensions of the anchors are shown in Figure 10. Figure 11 shows anchor No. 2 after having been pulled out of the ground.

Field test results are plotted in dimensionless form in Figures 6 and 7. The pullout load capacity for the shallow anchor was higher than the values predicted by Eq. 7 and Balla's equation. Since the thickness, b, of the field anchor is indeterminate, a direct comparison between the capacity of the deep anchor and that predicted by Eq. 11 is not justified.

CONCLUSIONS

1. The modes of failure for shallow (h/d < 6) and deep (h/d ≥ 6) anchors in dense sand are distinct and require separate analyses.

2. The pullout capacity for shallow and deep anchors in a dense sand can be represented by Eqs. 7 and 11, respectively.

ACKNOWLEDGMENTS

REFERENCES

1. Giffels, W. C., et al. Concrete Cylinder Anchors Proved for 345-KV Tower Line. Electrical World, Vol. 154, pp. 46-49, Dec. 19, 1960.
2. Markowsky, M., and Adams, J. I. Transmission Towers Anchored in Muskey. Electrical World, Vol. 155, pp. 36-37, 68, Feb. 20, 1961.
3. Hollander, W. H. Earth Anchors May Help You Prevent Pipe Flotation at River Crossings. Oil and Gas Jour., Vol. 56, pp. 98-101, May 26, 1958.
4. Poland, G. E. Anchoring a Tunnel in Sand. Civil Eng. p. 59, March 1960.
5. Belled Caissons Anchor Walls. Eng. News-Record, p. 28, May 11, 1961.
6. Cut Slope is Prestressed With Beams and Anchors. Eng. News-Record, Vol. 165, pp. 52-53, Oct. 20, 1960.
7. Tiebacks Remove Clutter in Excavation. Eng. News-Record, pp. 34-36, June 8, 1961.
8. Tie-Back Wall Braces Building Excavation. Construction Methods and Equipment, pp. 116-119, Nov. 1962.
9. Tied-Back Embankment Slides into Excavation. Eng. News-Record, p. 23, July 6, 1961.
10. Balla, A. The Resistance to Breaking Out of Mushroom Foundations for Pylons. Proc. 5th Int. Conf. on Soil Mech. and Found. Eng., Vol. 1, pp. 569-576, 1961.
11. Buckingham, E. On Physically Similar Systems. Phys. Rev., Vol. 4, pp. 354-376, 1914.
12. Bridgman, P. W. Dimensional Analysis. Connecticut, Yale Univ. Press, 1931.
13. Crandall, Leroy, and Associates, Consulting Foundation Engineers. Report of Foundation Investigation, Proposed Generating Station and Fuel Tank, Redondo Steam Station, Redondo Beach, California, for the Southern California Edison Company. Aug. 7, 1964.

Influence Chart for Vertical Stress Increases Due To Horizontal Shear Loadings

RICHARD D. BARKSDALE and MILTON E. HARR
Respectively, University Fellow and Professor of Civil Engineering,
Purdue University

An influence chart is presented for computing the vertical stress increase in the interior of a semi-infinite homogeneous isotropic elastic mass due to distributed horizontal shearing stresses applied at the surface. An example for a square surface area loaded with a uniform vertical stress and a wedge-shaped horizontal shearing stress is then worked out to illustrate the use of the influence chart. The mathematical development of the influence chart and a table summarizing the data required to construct the influence chart are also given.

•THE COMPUTATION of vertical stresses in a soil mass due to applied loadings is required for many problems in soil mechanics. Usually, as in the case of the consolidation settlement of foundations, only the stress due to vertical loadings are computed, and the effects of any horizontal shear stress that may be developed between the foundation base and the soil are neglected. This paper presents a simple graphical method for computing the vertical stresses in the interior of a semi-infinite elastic mass due to distributed, horizontal shearing stresses applied at the surface.

As was done by Newmark (1) for vertical loadings, the vertical stresses due to horizontal shearing loads are determined by drawing the foundation to a proper scale, and then counting the number of squares that the load covers when superimposed on an influence chart. Here also, the vertical stress is found by multiplying the horizontal shearing stress by the number of squares covered and a constant.

In the following sections the method of solution is presented, and an example is worked out illustrating the use of the influence chart. The detailed mathematical development of the influence chart and the data needed to construct the chart are given in the Appendix.

COMPUTATION OF VERTICAL STRESSES ON HORIZONTAL PLANES

The coordinate system used for the influence chart is shown in Figure 1. The x, y plane is taken as the horizontal surface of the semi-infinite soil mass, with the z axis extending vertically downward. Although any unidirectional distribution of horizontal shearing stress, q_h, is permissible in the x, y plane, the directional orientation of the stress must be considered. This requirement, however, is not restrictive; it is meant only to demonstrate the applicability of this procedure in solving problems.

The influence chart (Fig. 2) is constructed to give the increase in normal stress, $\Delta\sigma_z$, on a horizontal plane through point C', vertically beneath point C (Fig. 1) due to a horizontal shear loading applied on the surface. The usual soil mechanics sign convention is to be used for $\Delta\sigma_z$; a positive $\Delta\sigma_z$ stress change represents a compressive stress increase. As shown on Figures 1 and 2, horizontal shear loadings in quadrants 1 and 4 induce tensile $\Delta\sigma_z$ stresses at C', and shear loadings in quadrants 2 and 3 cause compressive stresses.
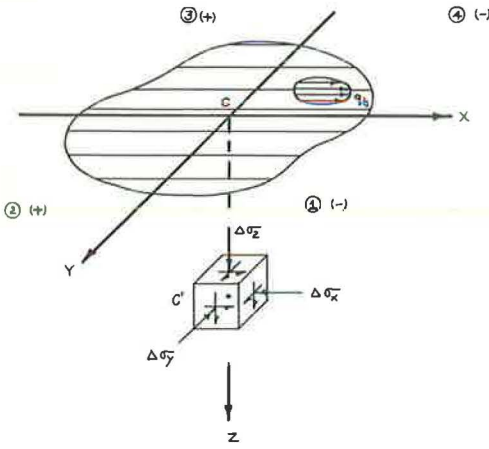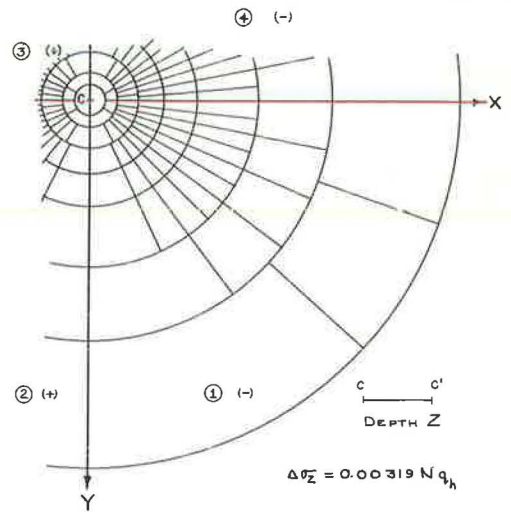
11

Figure 1. Notation used for influence chart.

Figure 2. Influence chart for increase in vertical stress due to horizontal shearing stress.

The influence chart represents the horizontal surface of the semi-infinite soil mass. The surface is divided into ring segments with the area of each ring such that if it is loaded with a uniform q_h shear stress, the stress increase $\Delta\sigma_z$ at C' will be the same absolute value as for any other loaded ring segment. Therefore, the contribution to the $\Delta\sigma_z$ stress of any loading can be accessed by counting the number of ring segments covered.

To determine the stress increase $\Delta\sigma_z$ at C' due to a uniform surface shear loading q_h, the area loaded is drawn on a sheet of tracing paper to a scale such that the depth below the surface to the point at which $\Delta\sigma_z$ is desired corresponds to the distance C C' (depth z) as given on the influence chart. The tracing paper is then placed over the influence chart and oriented so that the shear stress q_h points in the positive x direction, and the point C on the tracing paper under which the stress increase $\Delta\sigma_z$ is required coincides with point C on the influence chart (the origin). The algebraic sum, N, of the number of ring segments covered by the entire loading is determined with partially loaded ring segments included as corresponding fractions of the total ring segment. The vertical stress increase $\Delta\sigma_z$ (with correct sign) is then determined by:

$$\Delta\sigma_z = 0.00319\,Nq_h \qquad (1)$$

Since superposition is valid, any distribution of shear loading can be approximated as $q_h' + q_h'' + \dots + q_h^n$ with proper regard for signs, yielding the corresponding stress increase $\Delta\sigma_z' + \Delta\sigma_z'' + \Delta\sigma_z^n$. Of course, this procedure can be repeated for any number of points C to yield distributions of $\Delta\sigma_z$ on horizontal planes through any point C'.

ILLUSTRATIVE EXAMPLE

We seek to determine the increase in vertical stress at point C', 10 ft below the corner of the loaded 24- by 24-ft area shown in Figure 3. The load is composed of a uniform vertical pressure of 2 kips/sq ft, and a unidirectional horizontally distributed shearing stress that varies linearly in the positive x direction from 0 to 4 kips/sq ft.

Since the horizontal shear stress varies with x, a method of graphical integration must be used. As shown in Figures 3 and 4a, the loading (triangular in elevation) will be divided into four steps. Each step will be approximated as a uniformly distributed load. The four equivalent loadings are shown in Figures 4b to 4e. The additional loading introduced by this approach (dashed lines, Fig. 4a) makes the absolute value of the computed stress increase due to shear greater than the actual absolute value.
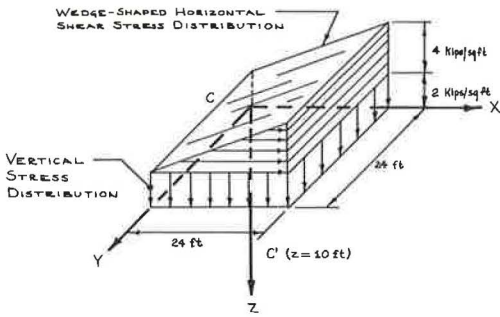
Figure 3. Vertical and horizontal loadings for illustrative example.
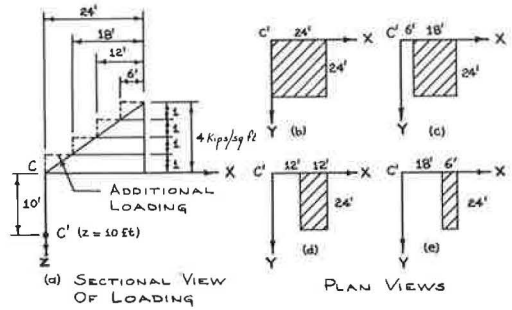
Figure 4. Division of triangular shear loading for graphical integration.

TABLE 1

TABULAR SOLUTION FOR CHANGE IN $\Delta\sigma_Z$ DUE TO HORIZONTAL SHEAR LOADINGS

Loaded Area[a]	q'_h (k/FT^2)	N	$\Delta\sigma_Z = \Sigma(0.00319\,Nq_h')$
b	1	-40.6	$\Delta\sigma_Z = 0.0319\,q_h'\,\Sigma N$
c	1	-25.8	$\Delta\sigma_Z = 0.00319\,(1)\,(-82.7)$
d	1	-12.0	$\Delta\sigma_Z = -0.264\,$kips/sqft (tension)
e	1	-4.3	
Total		-82.7	

[a]See Figure 4.

The precision of the graphical integration method increases with the number of incremental steps.

The next step is to plot the loadings of Figures 4b to 4e to the proper scale for use with the influence chart (Fig. 2). Whereas z = 10 ft for point C', the scale length for plotting the loadings is defined by the length C C' = 10 ft on Figure 2. By orienting each of the scaled plans so that point C coincides with the origin of the influence chart and then counting the ring segments, the results given in Table 1 are obtained. Since all ring segments are negative, the stress increase is tensile. Table 1 shows that the change in vertical stress, $\Delta\sigma_Z$, at point C' is -0.264 kips/sq ft (tension).

If eight load increments are used in the analysis instead of four, the computed vertical stress change would be $\Delta\sigma_Z = -0.234$ kips/sq ft, or a reduction of about 11 percent.

The increase in vertical stress due to the vertical loading was obtained from Newmark's chart (1) and was found to be +0.476 kips/sq ft. By combining the stress change due to the shear and vertical loadings, the net computed stress change at C' is $\Delta\sigma_Z$ = +0.242 kips/sq ft. For this example the error introduced by approximating the shear loading as shown in Figure 4a is on the unsafe side. However, by taking the incremental steps for this example on the inside of the actual loading, the error introduced would be on the safe side.

REFERENCES

1. Newmark, N. M. Influence Charts for Computation of Stresses in Elastic Foundations. Univ. of Illinois, Eng. Exp. Sta., Bull. No. 338, 1942.
2. Westergaard, H. M. Effects of a Change of Poisson's Ratio Analyzed by Twinned Gradients. Jour. Appl. Mech., p. A-115, Sept. 1940.
3. Love, A. E. H. A Treatise on the Mathematical Theory of Elasticity. P. 243. New York, Dover Publications.

Appendix

MATHEMATICAL DEVELOPMENT OF INFLUENCE CHART

The vertical stress increase $\Delta\sigma_Z$ at any point C' (Fig. 5) in a semi-infinite homogeneous isotropic elastic mass due to a concentrated horizontal surface loading Q_H was published in 1940 by Westergaard (2):

$$\sigma_Z = \frac{3Q_H}{2\pi R^2} \cos\psi \sin\theta \cos^2\theta \tag{2}$$

$$\sigma_Z = \frac{3Q_H}{2\pi R^5} \times z^2 \tag{3}$$

(According to A. E. H. Love (3), this problem received earlier attention by J. Boussinesq, V. Cerruti, and J. H. Mitchell.)

Of greater interest is the determination of the vertical stress increase at some depth z beneath point C (Fig. 6) due to a uniform horizontal shearing stress of intensity q_h, acting in the x direction over part of a circular segment. The following expressions are apparent from Figure 6:

$$dA_i = (\rho d\phi) \cdot d\rho \tag{4}$$

$$dQ_H = q_h \cdot dA_1 - q_h (\rho d\phi\, d\rho) \tag{5}$$

Substituting Eq. 5 into Eq. 3 gives for the differential of the vertical stress at some arbitrary constant depth z below C:
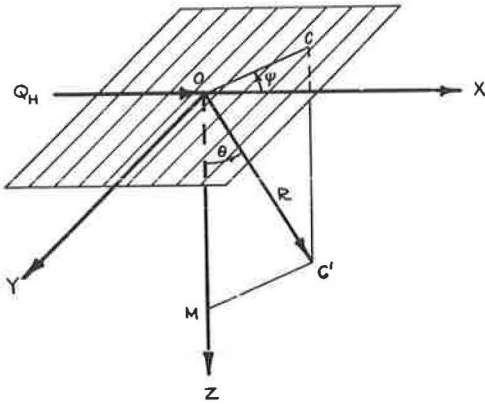
Figure 5. Notation used for determining vertical stress at point C' due to single horizontal load Q_H.

Note:
q_h = INTENSITY OF HORIZONTAL LOADING (IN X DIRECTION)
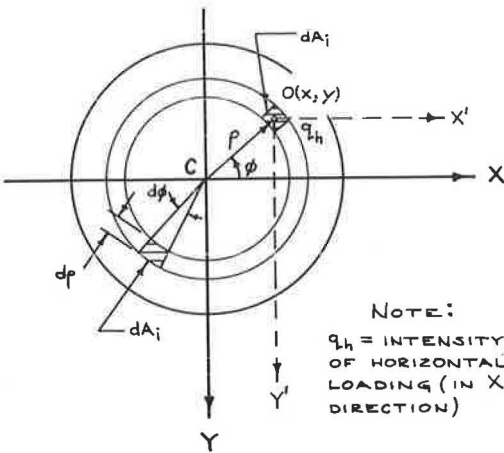
Figure 6. Plan view of horizontal surface loading on small area.

PLAN VIEW
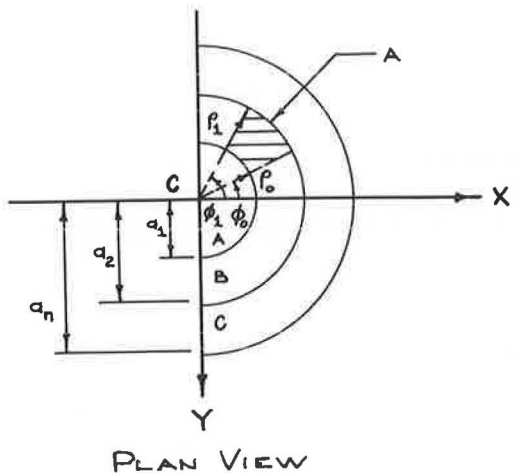
Figure 7. Notation used for Eq. 7b.

$$d\sigma_Z = \frac{3}{2\pi} \cdot q_h \frac{(\rho \, d\phi \, d\rho) \, (-\rho \cos \phi) \, (z^2)}{\left[\rho^2 \cos^2 \phi + \rho^2 \sin^2 \phi + z^2 \right]^{5/2}} \tag{6}$$

By simplifying and setting appropriate limits, we get:

$$\sigma_Z = -\frac{3}{2\pi} z^2 q_h \int_{\rho = \rho_0}^{\rho = \rho_1} \int_{\phi = \phi_0}^{\phi = \phi_1} \frac{\rho^2 \cos \phi \, d\phi \, d\rho}{\left[\rho^2 + z^2 \right]^{5/2}} \tag{7a}$$

which after integration becomes:

$$\sigma_Z = -\frac{q_h}{2\pi} [\sin \phi_1 - \sin \phi_0] \left[\left(\frac{1}{\left[1 + \left(\frac{z}{\rho_1} \right)^2 \right]} \right)^{3/2} - \left(\frac{1}{\left[1 + \left(\frac{z}{\rho_0} \right)^2 \right]} \right)^{3/2} \right] \tag{7b}$$

Eq. 7b is the expression for the vertical stress at some arbitrary depth z beneath point C due to shear loading (in the x direction) over the partial circular segment A, shown shaded in Figure 7.

The procedure used for developing the influence chart will be outlined. It is of advantage that Eq. 7b be expressed as:

$$\sigma_Z = -q_h \, KG \tag{8}$$

where

q_h = horizontal stress intensity in the x direction,
K = constant, and
$G = f (z, \phi_0, \phi_1, \rho_0, \rho_1)$.

If everywhere over an area such as Figure 7, each partial circular segment (A in the figure) is constructed so that its fraction of G is the same, with q_h and K known, σ_Z could be obtained by multiplying the number of segments covered by the loading and a constant.

The first step is to divide quadrants 1 and 4 (both having positive values of G) into concentric circles of radius a_n (Fig. 7) such that the area between each set of neighboring circles has the same fractional value of G. For any circle of radius a_n located in the half surface defined by quadrants 1 and 4, $\rho_0 = 0$, $\rho_1 = a_n$, $\phi_0 = -\pi/2$, $\phi_1 = \pi/2$. By letting $z = 1$ (unity), Eq. 7b becomes:

$$\sigma_Z = \frac{-q_h}{\pi} \left[\frac{1}{\left[1 + (1/a_n)^2 \right]^{3/2}} \right] \tag{9}$$

where

$$G = \frac{1}{\left[1 + 1/a_n^2 \right]^{3/2}} \tag{10}$$

and $K = 1/\pi$. Solving Eq. 10 for radius a_n gives:

TABLE 2

DEVELOPMENT OF INFLUENCE
CHART DATA

Ring No.	G (total for a_n)	a_n	G for Each Ring	G' No. of Ring Div.
A	0.01	0.22	0.01	1
B	0.05	0.40	0.04	4
C	0.19	0.70	0.14	14
D	0.39	1.07	0.20	20
E	0.59	1.54	0.20	20
F	0.79	2.42	0.20	20
G	0.89	3.52	0.10	10
H	0.95	5.36	0.06	6

$$a_n = \sqrt{\frac{1}{G^{2/3} - 1}} \tag{11}$$

Values of a_n given in Table 2 were obtained by assigning values for G and then solving Eq. 11 for the corresponding values of a_n. Each concentric ring may be divided into G' ring divisions where G' = 100 G. The value of G for any area loaded by q_h is now equal to the number of ring segments covered by the load divided by 100; i. e., G = G'/100. To do this requires that each ring segment be of such a size that G = 0.01. Hence, from Eqs. 7b and 8, considering partial ring segments:

$$G = 0.01 = \frac{1}{2} \left[\sin \phi_{m+1} - \sin \phi_m \right] \left[\frac{n}{100} \right] \tag{12}$$

where n is number of ring divisions for each concentric ring. Solving this expression for ϕ_{m+1} gives:

$$\phi_{m+1} = \arcsin \left[\frac{2}{n} + \sin \phi_m \right] \tag{13}$$

Thus, the angular location of the ring segment divisions (ϕ_{m+1}) can be obtained for any ϕ_m (starting with either $\phi_m = 0$ or $\phi_m = -\pi/2$). Then with this ϕ_{m+1} value taken as the new ϕ_m, the procedure is repeated until the ring is completely divided.

Table 3 summarizes the required data for constructing the influence chart. The scale used in constructing the a_n circles should be chosen such that z, the depth below the surface to the point at which the vertical stress increase is desired, is equal to 1 unit.

TABLE 3

SUMMARY OF INFLUENCE CHART DATA FOR QUADRANT 1
(ϕ in Degrees)

Radius (a_n)	0.22	0.40	0.70	1.07	1.54	2.42	3.52	5.36
Ring No.	A[a]	B	C	D	E	F	G	H
ϕ_0	-90	0	0	0	0	0	0	0
ϕ_1	90	30	8.2	5.7	5.7	5.7	11.5	19.5
ϕ_2		90	16.6	11.5	11.5	11.5	23.6	41.9
ϕ_3			25.4	17.5	17.5	17.5	36.9	90
ϕ_4			34.9	23.6	23.6	23.6	53.1	
ϕ_5			45.8	30.0	30.0	30.0	90	
ϕ_6			59.1	36.9	36.9	36.9		
ϕ_7			90	44.5	44.5	44.5		
ϕ_8				53.1	53.1	53.1		
ϕ_9				64.1	64.1	64.1		
ϕ_{10}				90	90	90		

[a]This ring segment goes from $\phi = -90°$ to $\phi = 90°$ (i.e., from $\phi = 0$ to $\phi = \pi/2$ is one-half a ring segment).

From Eq. 7b it follows that loadings in quadrants 1 and 4 induce negative vertical stresses and loadings in quadrants 2 and 3 correspond to positive vertical stresses. Recognizing that symmetry with respect to both the x and y axes is preserved, the tabulated data in Table 3 are sufficient to construct the entire influence chart wherein the vertical stress increase is given by:

$$\Delta \sigma_Z = \frac{1}{\pi} q_h \left(\frac{N}{100}\right) \tag{14}$$

where N is the algebraic sum of the segments covered by the horizontal loading.

Discussion

E. S. BARBER, Consulting Engineer, Soil Mechanics and Foundations—The paper is clearly presented and the chart is useful. However, a similar chart was already available. As been pointed out by the writer (4), the vertical stress from a shear load is the same as the shear stress from a vertical load. Therefore, Newmark's Figure 5 (1) is the same as the authors' chart except that Newmark's figure has finer divisions with a more convenient influence value of 0.001.

There is a similar correspondence between the shear stress from a shear load and the parallel horizontal normal stress (for Poisson's ratio equal to 0.5) from a normal load. Influence charts for horizontal normal stresses from a shear load are presented in the June 1965 issue of Public Roads.

For nonuniform loading the choice of approximations is important as illustrated in Figure 8 for the shear load in the authors' illustrative example. No. 1 is the authors' first approximation using columns instead of layers to reduce the number of blocks to be counted. The stress was calculated from Eq. 6 integrated over a rectangular area from 0 to Az in the x direction and from 0 to Bz in the y direction, giving, with q_h directed toward negative x,

$$\sigma_Z = \frac{q_h}{2\pi} \left(\frac{B}{\sqrt{1+B^2}} - \frac{B}{(1+A^2)\ \sqrt{1+A^2+B^2}}\right) \tag{15}$$

The resulting stress 0.271 is a little higher than the authors' value; an exact value is not to be expected from a graph. It is well to have two perpendicular depth scales on the influence chart to compensate for nonuniform shrinkage of the paper.
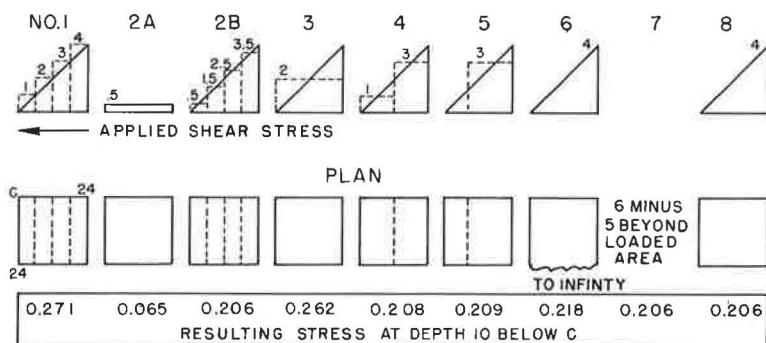
Figure 8. Various approximations of load distribution.

To make the total load of the approximation the same as the load to be approximated, No. 2A of Figure 8 is subtracted from No. 1 to obtain No. 2B. The resulting stress 0.206 is the same as No. 8 obtained by exact integration. For a stress increasing from 0 at x = 0 to q_h at x = Az:

$$\sigma_z = \frac{q_h}{2\pi} \left(\frac{\pi}{4A} - \frac{B}{(1 + A^2) \sqrt{1 + A^2 + B^2}} + \frac{1}{2A} \sin^{-1} \frac{A^2 B^2 - 1 - A^2 - B^2}{A^2 B^2 + 1 + A^2 + B^2} \right) \tag{16}$$

No. 3 is an unsatisfactory approximation but Nos. 4 and 5 are good. No. 4 balances over and under approximations and requires only two areas. No. 5 uses a single area with the centroid at the same location as the load to be approximated. No. 6 shows the small effect, in this case, of extending the loaded area to infinity.

Reference

4. Barber, E. S. Application of Triaxial Compression Test Results to the Calculation of Flexible Pavement Thickness. Highway Research Board Proc., Vol. 26, p. 37, 1946.

R. D. BARKSDALE and M. E. HARR, Closure—The authors thank Mr. Barber for pointing out that influence charts for computing the vertical stress at a point from a shear load on the surface are the same as those for computing the horizontal shear stress from a vertical load. This correspondence is implied by the Maxwell-Betti reciprocal theorem (5) since the semi-infinite solid is assumed to be elastic and follows Hooke's law.

The manner in which the load is approximated is certainly important in obtaining an accurate answer, as pointed out by Mr. Barber. The authors realized that the approximation used in the example would give an answer slightly on the high side and pointed this out in the discussion. The main purpose of the example was to illustrate the use of the chart and a simple numerical method of integration which could be applied to any load distribution.

Reference

5. Norris, C. H., and Wilbur, J. B. Elementary Structural Analysis. P. 390. New York, McGraw-Hill, 1960.

Effect of Variations in Poisson's Ratio on Soil Triaxial Testing

William M. Moore, Assistant Research Engineer, Texas Transportation Institute

The effect of variations in Poisson's ratio on the apparent elastic modulus and the apparent Poisson's ratio as determined from a conventional soil triaxial test is investigated. These parameters, the apparent elastic modulus and the apparent Poisson's ratio, are not the same as the true elastic constants appearing in Hooke's law. However, assuming that the soil behaves elastically, the true elastic constants, Young's modulus of elasticity and Poisson's ratio, can be determined by applying corrections to the apparent values obtained in triaxial testing. Curves showing the relationships between these true and apparent parameters are shown. Numerical solutions are presented for three values of Poisson's ratio and two values of height to diameter ratio.

•THE ANALYTIC problem of stresses and deformations in a short, elastic, right circular cylinder loaded between two flat loading plates has been considered several times in the literature (1, 2, 4, 5, 6). Because many materials are tested in this manner to evaluate their elastic properties, this problem must be thoroughly understood.

In the normal compression test, a cylinder tends to expand laterally as it is shortened by an axial load in a testing machine; however, frictional forces between the loading plates and the cylinder ends tend to prohibit this expansion. Exactly how the axial load is transmitted from the loading plate to the cylinder is unknown. It is known, however, that the ends of the cylinder are kept plane and that they are restricted to some large extent from radial expansion.

REVIEW OF LITERATURE AND BOUNDARY CONSIDERATIONS

Filon (1) first considered this problem. He assumed that the ends of the cylinder were kept plane and that no point on the ends could move in a radial direction, as if the ends were glued. He was unable to meet exactly these boundary conditions. Pickett (2) pointed out that Filon's solution allows all end points except those on the periphery to be displaced toward the center.

Considering the same boundary conditions that Filon attempted to meet, Pickett (2) solved this problem using a multiple Fourier technique. His graphical solution appears to be correct with possibly some numerical inaccuracies due to the slowly converging infinite series and the difficulty in hand computation (3).

Because using Pickett's solution was cumbersome for determining numerical values, D'Appolonia and Newmark (4) attacked the problem using a framework analogy. Their solution agrees reasonably well with Pickett's solution. However, it does not exactly meet all boundary conditions. Because their framework mesh size was rather large, some inaccuracies were to be expected.

Assuming slightly different boundary conditions, Balla (5) solved a similar problem. He assumed that the cylinder ends were kept plane, that the end shear stress distribution was linear, and that the radial displacement on the periphery at the ends varied inversely with a friction factor. When Balla's friction factor is the maximum value, the radial displacement at the periphery is zero.

Because the true end conditions are unknown, it is important that the end conditions in the standard compression test be investigated further. The use of porous stones for the end plates in the standard soil triaxial test, however, makes it difficult to imagine any slippage in this case. Thus, for this test the assumption of the boundary conditions — plane ends and no radial displacement on these ends—appears reasonable. These boundary conditions are used in this paper.

All of these solutions, except Balla's, have considered an elastic material with a Poisson's ratio of $\frac{1}{4}$; Balla used $\frac{1}{3}$. Considering the available solutions which may be applied to the triaxial test, two pertinent questions arise:

1. Are present interpretations valid, since measured values of Poisson's ratio have been reported which cover a considerable range of values (0. 1 to above 0. 5); and

2. How do variations in Poisson's ratio affect stresses in an elastic material compressed between two rough rigid loading plates?

It is the purpose of this paper to investigate the effect of Poisson's ratio on the "apparent modulus of elasticity" and the "apparent Poisson's ratio" estimated from a conventional triaxial test. The apparent modulus of elasticity is the average vertical stress (the total load acting on the loading plates divided by the cylinder cross-sectional area) divided by the average vertical unit strain (the change in height due to load divided by the original height). The apparent Poisson's ratio is the ratio of the average lateral unit strain at the cylinder mid-height (the increase in diameter divided by the original diameter) to the average vertical unit strain.

The difference between the apparent modulus and the true modulus, for the conditions assumed here, has been pointed out before in the literature. Edelman (6) reported that a cylinder with a height to diameter ratio equal to 1 and a Poisson's ratio of $\frac{1}{3}$ would have a measured apparent modulus approximately 5 percent larger than the true modulus. For a Poisson's ratio of $\frac{1}{4}$, D'Appolonia and Newmark (4) noted an error of approximately the same magnitude. In soil mechanics literature reviewed by the author, this phenomenon has not been mentioned. This is not at all surprising since the error reported seemed to be negligible when compared to the rather large variations usually observed in soil testing.

NOTATION

r, z, θ	=	cylindrical coordinate independent variables;
u, w	=	displacements in r and z directions, respectively;
$\epsilon_r, \epsilon_z, \epsilon_\theta$	=	unit normal strains in subscript direction;
γ_{rz}	=	unit shear strain in r-z plane;
$\sigma_r, \sigma_z, \sigma_\theta$	=	unit normal stress in the subscript direction;
τ_{rz}	=	unit shear stress in r-z plane;
D	=	diameter of cylinder;
H	=	height of cylinder;
P	=	total axial load on cylinder;
Δ	=	shortening in height due to load;
μ	=	Poisson's ratio;
E	=	Young's modulus of elasticity;
σ_1	=	P divided by cylinder cross-sectional area; and
σ_3	=	lateral pressure acting on cylinder at r = D/2.

THEORY

The fundamental equations to be satisfied are as follows (Fig. 1):

Equations of equilibrium

$$\frac{\partial \sigma_r}{\partial r} + \frac{\partial \tau_{rz}}{\partial z} + \frac{\sigma_r - \sigma_\theta}{r} = 0 \tag{1}$$

$$\frac{\partial \tau_{rz}}{\partial r} + \frac{\partial \sigma_z}{\partial z} + \frac{\tau_{rz}}{r} = 0 \qquad (2)$$

Equations representing Hooke's law

$$\epsilon_z = \frac{\partial w}{\partial z} = \frac{\sigma_z - \mu (\sigma_r + \sigma_\theta)}{E} \qquad (3)$$

$$\epsilon_z = \frac{\partial u}{\partial r} = \frac{\sigma_r - \mu (\sigma_z + \sigma_\theta)}{E} \qquad (4)$$

$$\epsilon_\theta = \frac{u}{r} = \frac{\sigma_\theta - \mu (\sigma_z + \sigma_r)}{E} \qquad (5)$$

$$\gamma_{rz} = \frac{\partial w}{\partial r} + \frac{\partial u}{\partial z} =$$

$$\frac{2 (1 + \mu) \tau_{rz}}{E} \qquad (6)$$

Hooke's law can be rewritten in the following form:

$$\sigma_z = \frac{E \mu}{(1 + \mu) (1 - 2\mu)}$$

$$\left[\left(\frac{1 - \mu}{\mu} \right) \frac{\partial w}{\partial z} + \frac{\partial u}{\partial r} + \frac{u}{r} \right] (7)$$
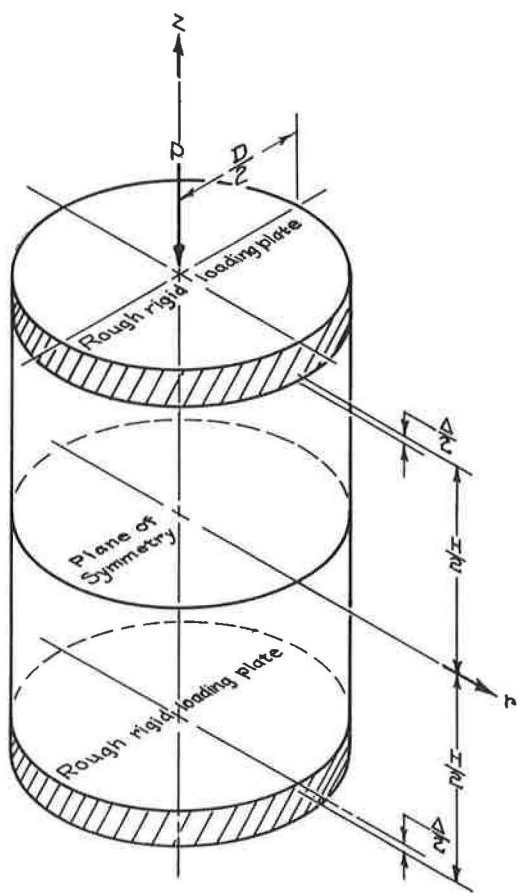
Figure 1. Loading system.

$$\sigma_r = \frac{E \mu}{(1 + \mu) (1 - 2\mu)} \left[\frac{\partial w}{\partial z} + \left(\frac{1 - \mu}{\mu} \right) \frac{\partial u}{\partial r} + \frac{u}{r} \right] \qquad (8)$$

$$\sigma_\theta = \frac{E \mu}{(1 + \mu) (1 - 2\mu)} \left[\frac{\partial w}{\partial z} + \frac{\partial u}{\partial r} + \left(\frac{1 - \mu}{\mu} \right) \frac{u}{r} \right] \qquad (9)$$

$$\tau_{rz} = \frac{E}{2(1 + \mu)} \left[\frac{\partial w}{\partial r} + \frac{\partial u}{\partial z} \right] \qquad (10)$$

By combining Eqs. 7 through 10 with Eqs. 1 and 2, the equilibrium equations can be rewritten as follows:

$$\frac{\partial^2 w}{\partial r \, \partial z} + 2(1 - \mu) \left[\frac{\partial^2 u}{\partial r^2} + \frac{1}{r} \frac{\partial u}{\partial r} - \frac{u}{r^2} \right] + (1 - 2\mu) \frac{\partial^2 u}{\partial z^2} = 0 \qquad (11)$$

$$(1 - 2\mu) \left[\frac{\partial^2 w}{\partial r^2} + \frac{1}{r} \frac{\partial w}{\partial r} \right] + 2(1 - \mu) \frac{\partial^2 w}{\partial z^2} + \frac{\partial^2 u}{\partial r\,\partial z} + \frac{1}{r} \frac{\partial u}{\partial z} = 0 \qquad (12)$$

The assumed boundary conditions are:

$$\sigma_r = 0, \text{ when } r = D/2^* \qquad (13a)$$

$$\tau_{rz} = 0, \text{ when } r = D/2 \qquad (14)$$

$$w = \Delta/2, \text{ when } z = H/2 \qquad (15a)$$

$$u = 0, \text{ when } z = H/2 \qquad (16)$$

On writing the first two boundary conditions in terms of u and w,

$$\frac{\partial w}{\partial z} + \left(\frac{1 - \mu}{\mu} \right) \frac{\partial u}{\partial r} + \frac{u}{r} = 0, \text{ when } r = D/2 \qquad (17a)$$

$$\frac{\partial w}{\partial r} + \frac{\partial u}{\partial z} = 0, \text{ when } r = D/2 \qquad (18)$$

The problem is reduced to finding the solution to Eqs. 11 and 12 (considering u and w only) which satisfies the boundary conditions set in Eqs. 15a, 16, 17a, and 18. Since stresses are not considered in the solution, they must be determined using Hooke's law (Eqs. 7 through 10) after the solution for u and w is obtained.

If the equilibrium equations (Eqs. 11 and 12) and boundary equations (Eqs. 15a, 16, 17a, and 18) are rewritten in terms of u and w, for a given height to diameter ratio (H/D), the solution to these equations in not dependent on the modulus of elasticity (E) but only on Poisson's ratio (μ) and the change in height (Δ). The only way E enters the solution is through Hooke's law in the stress calculations (Eqs. 7 through 10). At any point in the cylinder, the displacements and the strains are directly proportional to Δ. Therefore, the stresses at any point are directly proportional to $E\Delta$ and the constant of proportionality for each stress component is a function of r, z, and μ.

Considering the principle of superposition in elasticity theory, it is evident that confining pressure has no influence on the apparent modulus of elasticity or the apparent Poisson's ratio. The measurements made in testing to determine these quantities are the changes in total load and the corresponding changes in diameter at mid-height while holding the confining pressure constant.

Confining pressure can be introduced as a consideration in the solution by changing only boundary Eqs. 13a and 15a:

$$\sigma_r = \sigma_3, \text{ when } r = D/2 \qquad (13b)$$

$$w = 0, \text{ when } z = H/2 \qquad (15b)$$

On writing Eq. 13b in terms of u and w, Eq. 17 is replaced with the following:

$$\frac{\partial w}{\partial z} + \left(\frac{1 - \mu}{\mu} \right) \frac{\partial u}{\partial r} + \frac{u}{r} = \frac{\sigma_3(1 + \mu)(1 - 2\mu)}{\mu E}, \text{ when } r = D/2 \qquad (17b)$$

These boundary conditions result in a total load P of less than σ_3 times the cylinder cross-sectional area. The resultant solution is not for the condition of the usual tri-

---

*Introducing confining pressure as a boundary consideration at this point will only tend to make the problem more difficult. It will be treated later and the reasons for delay will be apparent.
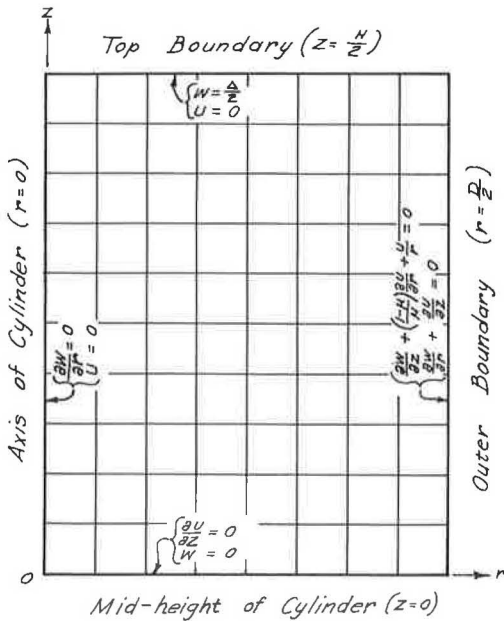
Figure 2. Equation system.

TABLE 1

H/D	μ	Apparent μ	Apparent E/True E
1	0.15	0.151	1.013
1	0.25	0.260	1.038
1	0.33	0.356	1.071
1	0.40	0.452	1.117
1	0.45	0.537	1.167
1	0.48	0.608	1.229
2	0.15	0.152	1.006
2	0.25	0.257	1.018
2	0.33	0.345	1.034
2	0.40	0.429	1.055
2	0.45	0.499	1.078
2	0.48	0.563	1.119

axial test in which the confining pressure acts on both the sides and loading plates. However, employing the principle of superposition the solutions for the unconfined cylinder and the confined cylinder can be combined for this condition or any other particular condition desired.

PROCEDURE

The procedure used to study this problem, finite difference equations solved by iterative methods, is the same as that used by Dingwall and Scrivner (7) to solve a rather complex embankment problem. This approximate procedure can be quite accurate, as Dingwall and Scrivner pointed out: "... any desired degree of accuracy may be obtained by making the mesh size sufficiently small." To perform the iterative calculations on a small mesh size for this research, an IBM 709 computer was used to obtain a set of solutions for various Poisson's ratios.

Rather than use a single stress function, as used by Dingwall and Scrivner, Eqs. 11 and 12 were used to solve for u and w, respectively, at all interior nodal points. The boundary conditions, Eqs. 15a, 16, 17a, and 18 along with symmetry conditions were used on appropriate boundaries (Fig. 2). Basically the procedure consists of successively changing the values of u and w at each nodal point as required to satisfy the appropriate equations written in finite difference form, until the changes become negligible. In writing the finite difference equations at any nodal point, it was assumed that the functions representing u and w in the neighborhood of the point could be approximated by a parabola.

Solutions for unconfined cylinders of six different Poisson's ratios, 0.15, 0.25, 0.33, 0.40, 0.45, and 0.48, were obtained for both H/D equal to 1 and H/D equal to 2. Stresses and displacements from these solutions for three different Poisson's ratios, 0.25, 0.40, and 0.45, for both H/D equal to 1 and H/D equal to 2 are shown in Appendices A and B. Solutions for confined cylinders of three different Poisson's ratios, 0.25, 0.40, and 0.45, were obtained for H/D equal to 2. Stresses and displacements from these solutions are shown in Appendix C. To obtain the solutions reported here a square grid was used with a mesh size of D/64. Convergence was assumed when changes in the maximum deformations were confined to the sixth significant figure; all other changes in deformations were smaller.

The total force, P, was calculated for each z by numerical integration. The value of P at z = H/4 for each value of μ remained approximately constant as the mesh size
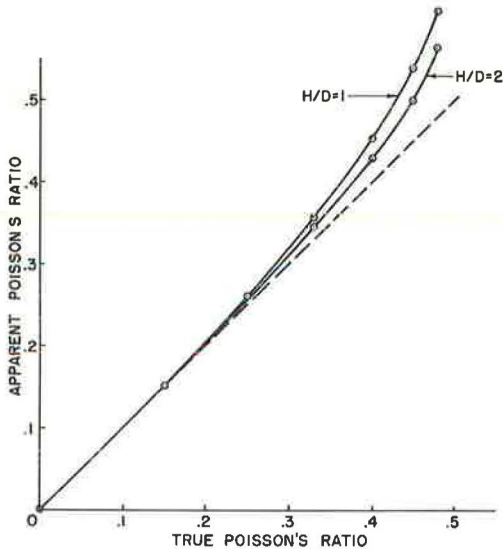
Figure 3. Apparent Poisson's ratio vs true Poisson's ratio.

Figure 4. Ratio-apparent E/true E vs Poisson's ratio.

was decreased; at other values of z it varied somewhat. The average vertical stress, σ_1, used to compute the apparent moduli (Table 1) and the stress ratios (Appendices A, B and C) for each μ, was obtained by dividing P at z = H/4 by the cross-sectional area.

DISCUSSION

The numerical values (Appendices A and B) for the shear stress (τ_{rz}) on the ends of the cylinder are not large when compared to the corresponding vertical normal stress (σ_z). Thus, for the conventional triaxial test it appears that sufficient friction would exist to restrain end expansion, and the end conditions assumed here are justified.

The author was unable to obtain a solution to this problem for a cylinder with a Poisson's ratio equal to $\frac{1}{2}$. It appeared (Eqs. 7 through 9) that for μ equal to $\frac{1}{2}$, the normal stresses would be infinite. In addition, the computer time required for convergence on the small mesh became prohibitive as μ approached the limit of $\frac{1}{2}$. Therefore, for practical considerations the results shown in Table 1 and plotted in Figures 3 and 4 do not show results for values of Poisson's ratios larger than 0.48. However, it is evident that the apparent modulus of elasticity and the apparent Poisson's ratio are both increasing very rapidly as μ approaches $\frac{1}{2}$. Figures 3 and 4 show that for H/D equal to 2 and μ less than $\frac{1}{3}$ the corrections in the commonly measured elastic parameters are less than 5 percent. However, when μ equals 0.48, the correction for E is approximately 12 percent and for μ approximately 17 percent. These corrections appear to become quite large as μ approaches $\frac{1}{2}$.

The following is an example of how the true elastic parameters could be estimated from the data reported here. If in a triaxial test with H/D equal to 2 an apparent Poisson's ratio of 0.52 is measured, the true μ is 0.44 according to Figure 3. Then from Figure 4 the ratio of the apparent to true modulus is 1.07. Thus, the true elastic modulus is the measured apparent modulus divided by 1.07.

CONCLUSIONS

1. The boundary conditions—plane ends and no radial displacement on these ends—appear to be realistic assumptions for an ideal elastic soil tested in a conventional triaxial test.

2. The elastic parameters measured in triaxial testing are not the elastic parameters (E and μ) expressed in Hooke's law.
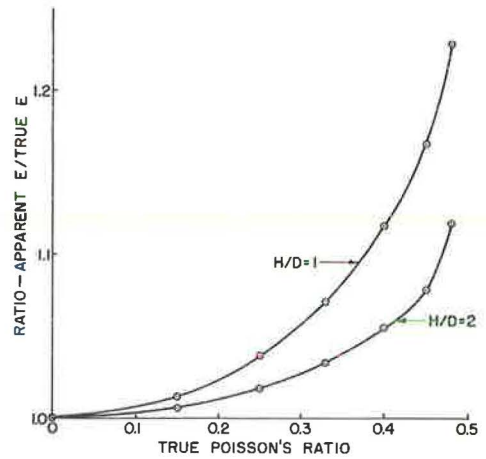
3. The true elastic parameters (E and μ) expressed in Hooke's law can be obtained from the conventional triaxial test by applying corrections to the measured apparent parameters (Figs. 3 and 4), providing that the material tested behaves elastically.

4. The upper limit of $\frac{1}{2}$ for Poisson's ratio in the theory of elasticity should be studied further as related to rigid boundaries.

ACKNOWLEDGMENTS

REFERENCES

1. Filon, L. N. G. The Elastic Equilibrium of Circular Cylinders Under Certain Practical Systems of Load. Philosophical Trans., Royal Soc. (London), Series A, Vol. 198, 1902.
2. Pickett, G. Application of the Fourier Method to the Solution of Certain Boundary Problems in the Theory of Elasticity. Jour. Appl. Mech. Vol. 2, 1944.
3. Pickett, G. Personal communication, May 1964.
4. D'Appolonia, E., and Newmark, N. M. A Method for Solution of the Restrained Cylinder Under Axial Compression. Proc. 1st U. S. Nat. Conf. of Appl. Mech., ASME, 1951.
5. Balla, A. Stress Conditions in Triaxial Compression. Trans. ASCE, Vol. 126, Pt. 1, 1961.
6. Edelman, F. On the Compression of a Short Cylinder Between Rough End Blocks. Quarterly of Appl. Math., Brown Univ., Vol. 7, No. 3, Oct. 1949.
7. Dingwall, J. C., and Scrivner, F. H. Application of the Elastic Theory to Highway Embankments by Use of Difference Equations. Highway Research Board, Proc., Vol. 33, pp. 474-482, 1954.
8. Timoshenko, S., and Goodier, J. N. Theory of Elasticity. 2nd ed. New York, McGraw-Hill, 1951.

Appendix A

STRESSES AND DISPLACEMENTS FOR UNCONFINED COMPRESSION, H/D = 1

TABLE A-1
$\mu = 0.25$, $\sigma_3 = 0$, H/D =1

2z/H	2r/D					2r/D				
	0	0.25	0.50	0.75	1	0	0.25	0.50	0.75	1
	u/Δ					w/Δ				
1	0	0	0	0	0	-0.500	-0.500	-0.500	-0.500	-0.500
0.75	0	0.015	0.032	0.054	0.085	-0.394	-0.393	-0.392	-0.385	-0.357
0.50	0	0.026	0.053	0.084	0.115	-0.271	-0.270	-0.266	-0.257	-0.240
0.25	0	0.032	0.064	0.096	0.127	-0.137	-0.137	-0.134	-0.128	-0.121
0	0	0.033	0.067	0.099	0.130	0	0	0	0	0
	τ_{rz}/σ_1					σ_z/σ_1				
1	0	0.048	0.101	0.173	0.686	0.892	0.893	0.898	0.932	3.130
0.75	0	0.039	0.076	0.092	0	0.980	0.982	0.994	1.022	0.924
0.50	0	0.020	0.030	0.018	0	1.039	1.038	1.033	1.006	0.908
0.25	0	0.006	0.007	0.000	0	1.065	1.059	1.036	0.993	0.925
0	0	0	0	0	0	1.072	1.064	1.037	0.989	0.933
	σ_r/σ_1					σ_θ/σ_1				
1	0.297	0.298	0.299	0.311	1.043	0.297	0.298	0.299	0.311	1.043
0.75	0.177	0.170	0.146	0.082	0	0.177	0.174	0.163	0.138	0.066
0.50	0.083	0.076	0.053	0.018	0	0.083	0.079	0.066	0.041	0.005
0.25	0.030	0.026	0.015	0.004	0	0.030	0.027	0.017	0.003	-0.013
0	0.014	0.011	0.005	0.001	0	0.014	0.011	0.003	-0.007	-0.017

TABLE A-2
$\mu = 0.40$, $\sigma_3 = 0$, H/D =1

2z/H	2r/D					2r/D				
	0	0.25	0.50	0.75	1	0	0.25	0.50	0.75	1
	u/Δ					w/Δ				
1	0	0	0	0	0	-0.500	-0.500	-0.500	-0.500	-0.500
0.75	0	0.029	0.060	0.101	0.154	-0.420	-0.419	-0.416	-0.406	-0.359
0.50	0	0.048	0.099	0.152	0.203	-0.299	-0.298	-0.291	-0.275	-0.246
0.25	0	0.058	0.116	0.172	0.221	-0.155	-0.153	-0.148	-0.138	-0.126
0	0	0.061	0.121	0.177	0.226	0	0	0	0	0
	τ_{rz}/σ_1					σ_z/σ_1				
1	0	0.078	0.165	0.280	1.236	0.862	0.859	0.853	0.875	6.975
0.75	0	0.061	0.119	0.142	0	1.002	1.002	1.006	1.025	0.811
0.50	0	0.029	0.042	0.021	0	1.092	1.086	1.066	1.004	0.824
0.25	0	0.008	0.007	-0.005	0	1.127	1.114	1.071	0.985	0.867
0	0	0	0	0	0	1.136	1.120	1.069	0.981	0.885
	σ_r/σ_1					σ_θ/σ_1				
1	0.574	0.572	0.569	0.583	4.650	0.574	0.572	0.569	0.583	4.650
0.75	0.333	0.320	0.274	0.156	0	0.333	0.325	0.297	0.233	0.048
0.50	0.154	0.140	0.099	0.037	0	0.154	0.144	0.112	0.053	-0.033
0.25	0.055	0.047	0.028	0.009	0	0.055	0.046	0.023	-0.012	-0.049
0	0.025	0.020	0.010	0.003	0	0.025	0.018	-0.002	-0.028	-0.051

TABLE A-3

$\mu = 0.45, \ \sigma_3 = 0, \ H/D = 1$

2z/H	2r/D					2r/D				
	0	0.25	0.50	0.75	1	0	0.25	0.50	0.75	1
	u/Δ					w/Δ				
1	0	0	0	0	0	-0.500	-0.500	-0.500	-0.500	-0.500
0.75	0	0.035	0.073	0.120	0.180	-0.434	-0.434	-0.431	-0.419	-0.367
0.50	0	0.059	0.119	0.182	0.239	-0.315	-0.314	-0.307	-0.288	-0.254
0.25	0	0.071	0.140	0.206	0.262	-0.164	-0.163	-0.157	-0.146	-0.130
0	0	0.074	0.146	0.212	0.268	0	0	0	0	0
	τ_{rz}/σ_1					σ_z/σ_1				
1	0	0.091	0.188	0.315	1.378	0.864	0.858	0.843	0.853	11.966
0.75	0	0.068	0.133	0.161	0	1.021	1.017	1.011	1.016	0.757
0.50	0	0.032	0.049	0.026	0	1.120	1.110	1.081	1.004	0.790
0.25	0	0.009	0.009	-0.005	0	1.160	1.143	1.090	0.988	0.845
0	0	0	0	0	0	1.171	1.152	1.090	0.985	0.868
	σ_r/σ_1					σ_θ/σ_1				
1	0.707	0.702	0.690	0.698	9.791	0.707	0.702	0.690	0.698	9.791
0.75	0.406	0.390	0.334	0.201	0	0.406	0.394	0.356	0.273	0.032
0.50	0.189	0.173	0.124	0.051	0	0.189	0.175	0.134	0.060	-0.053
0.25	0.069	0.059	0.035	0.011	0	0.069	0.058	0.027	-0.020	-0.068
0	0.034	0.027	0.012	0.003	0	0.034	0.024	-0.003	-0.039	-0.069

Appendix B

STRESSES AND DISPLACEMENTS FOR UNCONFINED COMPRESSION, H/D = 2

TABLE B-1

$\mu = 0.25, \ \sigma_3 = 0, \ H/D = 2$

2z/H	2r/D					2r/D				
	0	0.25	0.50	0.75	1	0	0.25	0.50	0.75	1
	u/Δ					w/Δ				
1	0	0	0	0	0	-0.500	-0.500	-0.500	-0.500	-0.500
0.875	0	0.007	0.015	0.026	0.042	-0.448	-0.448	-0.447	-0.443	-0.430
0.750	0	0.012	0.025	0.035	0.056	-0.389	-0.388	-0.386	-0.381	-0.372
0.625	0	0.015	0.030	0.044	0.062	-0.325	-0.324	-0.322	-0.318	-0.313
0.500	0	0.016	0.032	0.047	0.064	-0.260	-0.259	-0.257	-0.254	-0.252
0.375	0	0.016	0.033	0.048	0.064	-0.194	-0.194	-0.192	-0.191	-0.190
0.250	0	0.016	0.033	0.049	0.064	-0.129	-0.129	-0.128	-0.127	-0.127
0.125	0	0.016	0.032	0.048	0.064	-0.064	-0.064	-0.064	-0.064	-0.064
0	0	0.016	0.033	0.048	0.064	0	0	0	0	0
	τ_{rz}/σ_1					σ_z/σ_1				
1	0	0.046	0.098	0.170	0.683	0.886	0.887	0.895	0.932	3.118
0.875	0	0.037	0.072	0.089	0	0.969	0.973	0.989	1.021	0.926
0.750	0	0.016	0.024	0.013	0	1.022	1.024	1.026	1.007	0.915
0.625	0	0.001	-0.002	-0.008	0	1.039	1.037	1.026	0.997	0.943
0.500	0	-0.005	-0.010	-0.011	0	1.035	1.031	1.018	0.995	0.967
0.375	0	-0.005	-0.009	-0.008	0	1.025	1.022	1.011	0.996	0.984
0.250	0	-0.004	-0.006	-0.005	0	1.016	1.014	1.007	0.999	0.993
0.125	0	-0.002	-0.003	-0.002	0	1.011	1.009	1.005	1.000	0.998
0	0	0	0	0	0	1.009	1.008	1.004	1.000	0.999
	σ_r/σ_1					σ_θ/σ_1				
1	0.295	0.296	0.298	0.311	1.039	0.295	0.296	0.298	0.311	1.039
0.875	0.179	0.172	0.147	0.082	0	0.179	0.176	0.165	0.140	0.068
0.750	0.087	0.079	0.054	0.018	0	0.087	0.083	0.070	0.045	0.010
0.625	0.033	0.028	0.016	0.005	0	0.033	0.030	0.021	0.008	-0.006
0.500	0.007	0.006	0.003	0.001	0	0.007	0.006	0.002	-0.003	-0.008
0.375	-0.002	-0.002	-0.002	0.000	0	-0.002	-0.003	-0.004	-0.006	-0.007
0.250	-0.005	-0.004	-0.003	-0.001	0	-0.005	-0.005	-0.005	-0.005	-0.004
0.125	-0.005	-0.004	-0.003	-0.001	0	-0.005	-0.005	-0.005	-0.004	-0.003
0	-0.005	-0.004	-0.002	-0.001	0	-0.005	-0.005	-0.004	-0.004	-0.003

TABLE B-2

$\mu = 0.4,\ \sigma_3 = 0,\ H/D = 2$

2z/H	2r/D						2r/D				
	0	0.25	0.50	0.75	1		0	0.25	0.50	0.75	1
	u/Δ						w/Δ				
1	0	0	0	0	0		-0.500	-0.500	-0.500	-0.500	-0.500
0.875	0	0.013	0.027	0.046	0.072		-0.463	-0.463	-0.461	-0.456	-0.434
0.750	0	0.022	0.045	0.070	0.094		-0.409	-0.408	-0.403	-0.395	-0.381
0.625	0	0.026	0.052	0.079	0.103		-0.344	-0.342	-0.338	-0.330'	-0.323
0.500	0	0.028	0.055	0.081	0.106		-0.275	-0.273	-0.270	-0.265	-0.261
0.375	0	0.028	0.055	0.082	0.107		-0.205	-0.204	-0.202	-0.199	-0.197
0.250	0	0.028	0.055	0.081	0.107		-0.136	-0.136	-0.134	-0.133	-0.132
0.125	0	0.027	0.054	0.081	0.107		-0.068	-0.068	-0.067	-0.067	-0.066
0	0	0.027	0.054	0.081	0.107		0	0	0	0	0
	τ_{rz}/σ_1						σ_z/σ_1				
1	0	0.073	0.157	0.273	1.223		0.843	0.842	0.843	0.870	6.889
0.875	0	0.056	0.112	0.136	0		0.975	0.978	0.992	1.020	0.812
0.750	0	0.022	0.032	0.012	0		1.054	1.054	1.047	1.002	0.835
0.625	0	-0.002	-0.010	-0.019	0		1.075	1.069	1.046	0.989	0.895
0.500	0	-0.010	-0.019	-0.021	0		1.065	1.057	1.032	0.990	0.994
0.375	0	-0.010	-0.016	-0.014	0		1.047	1.040	1.022	0.996	0.975
0.250	0	-0.007	-0.010	-0.008	0		1.032	1.028	1.016	1.001	0.992
0.125	0	-0.003	-0.005	-0.004	0		1.024	1.021	1.013	1.004	1.001
0	0	0	0	0	0		1.021	1.018	1.012	1.005	1.004
	σ_r/σ_1						σ_θ/σ_1				
1	0.562	0.561	0.562	0.580	4.599		0.562	0.561	0.562	0.580	4.599
0.875	0.333	0.320	0.272	0.155	0		0.333	0.325	0.299	0.236	0.053
0.750	0.159	0.145	0.101	0.038	0		0.159	0.150	0.120	0.063	0.000
0.625	0.058	0.050	0.030	0.010	0		0.058	0.052	0.032	0.002	-0.032
0.500	0.011	0.009	0.004	0.002	0		0.011	0.008	0.001	-0.014	-0.025
0.375	-0.006	-0.005	-0.004	-0.001	0		-0.006	-0.007	-0.010	-0.014	-0.016
0.250	-0.010	-0.009	-0.006	-0.002	0		-0.010	-0.011	-0.011	-0.013	-0.013
0.125	-0.011	-0.009	-0.006	-0.002	0		-0.011	-0.011	-0.010	-0.010	-0.008
0	-0.010	-0.009	-0.006	-0.002	0		-0.010	-0.010	-0.009	-0.008	-0.005

TABLE B-3

$\mu = 0.45,\ \sigma_3 = 0,\ H/D = 2$

2z/H	2r/D						2r/D				
	0	0.25	0.50	0.75	1		0	0.25	0.50	0.75	1
	u/Δ						w/Δ				
1	0	0	0	0	0		-0.500	-0.500	-0.500	-0.500	-0.500
0.875	0	0.015	0.017	0.029	0.081		-0.472	-0.471	-0.469	-0.463	-0.440
0.750	0	0.025	0.043	0.069	0.107		-0.420	-0.419	-0.414	-0.404	-0.388
0.625	0	0.030	0.057	0.087	0.117		-0.356	-0.354	-0.348	-0.340	-0.330
0.500	0	0.032	0.063	0.093	0.122		-0.285	-0.284	-0.279	-0.273	-0.268
0.375	0	0.032	0.064	0.094	0.124		-0.213	-0.212	-0.209	-0.206	-0.203
0.250	0	0.032	0.064	0.095	0.124		-0.142	-0.141	-0.139	-0.137	-0.136
0.125	0	0.032	0.063	0.094	0.125		-0.071	-0.070	-0.070	-0.069	-0.068
0	0	0.032	0.063	0.094	0.125		0	0	0	0	0
	τ_{rz}/σ_1						σ_z/σ_1				
1	0	0.082	0.175	0.300	1.342		0.827	0.824	0.818	0.836	11.648
0.875	0	0.061	0.122	9.150	0		0.971	0.972	0.979	0.997	0.750
0.750	0	0.024	0.035	0.014	0		1.058	1.055	1.044	0.989	0.796
0.625	0	-0.002	-0.011	-0.022	0		1.083	1.076	1.048	0.981	0.872
0.500	0	-0.011	-0.022	-0.023	0		1.075	1.066	1.038	0.988	0.933
0.375	0	-0.011	-0.018	-0.017	0		1.059	1.051	1.030	0.999	0.973
0.250	0	-0.007	-0.012	-0.010	0		1.045	1.040	1.025	1.007	0.996
0.125	0	-0.004	-0.006	-0.004	0		1.037	1.033	1.024	1.003	1.008
0	0	0	0	0	0		1.034	1.031	1.023	1.014	1.011
	σ_r/σ_1						σ_θ/σ_1				
1	0.677	0.674	0.670	0.684	9.531		0.677	0.674	0.670	0.684	9.531
0.875	0.399	0.383	0.328	0.196	0		0.399	0.389	9.354	0.275	0.038
0.750	0.193	0.176	0.126	0.051	0		0.193	0.181	0.143	0.072	-0.038
0.625	0.073	0.063	0.039	0.014	0		0.073	0.064	0.039	0.001	-0.043
0.500	0.015	0.012	0.006	0.002	0		0.015	0.011	-0.002	-0.018	-0.032
0.375	-0.008	-0.007	-0.006	-0.002	0		-0.008	-0.009	-0.014	-0.019	-0.021
0.250	-0.015	-0.013	-0.009	-0.003	0		-0.015	-0.015	-0.016	-0.016	-0.014
0.125	-0.016	-0.014	-0.009	-0.004	0		-0.016	-0.015	-0.015	-0.013	-0.009
0	-0.016	-0.014	-0.009	-0.004	0		-0.016	-0.015	-0.014	-0.012	-0.008

Appendix C

STRESS AND DISPLACEMENTS FOR CONFINING PRESSURE WITH NO AXIAL COMPRESSION

TABLE C-1

$\mu = 0.25$, $\sigma_1/\sigma_3 = 0.455$, $H/D = 2$

2z/H	2r/D					2r/D				
	0	0.25	0.50	0.75	1	0	0.25	0.50	0.75	1
	$uE/D\sigma_3$					$wE/D\sigma_3$				
1	0	0	0	0	0	0	0	0	0	0
0.875	0	0.035	0.076	0.130	0.209	0.055	0.053	0.048	0.030	-0.038
0.750	0	0.062	0.128	0.203	0.280	0.070	0.067	0.055	0.029	-0.014
0.625	0	0.076	0.153	0.232	0.309	0.062	0.058	0.046	0.025	0.003
0.500	0	0.081	0.162	0.241	0.319	0.047	0.044	0.034	0.021	0.010
0.375	0	0.082	0.163	0.243	0.321	0.032	0.030	0.024	0.016	0.012
0.250	0	0.082	0.163	0.243	0.321	0.019	0.018	0.015	0.011	0.010
0.125	0	0.082	0.162	0.242	0.321	0.009	0.009	0.007	0.006	0.005
0	0	0.081	0.162	0.242	0.321	0	0	0	0	0
	τ_{rz}/σ_3					σ_z/σ_3				
1	0	0.117	0.250	0.436	1.738	0.750	0.746	0.728	0.638	-4.938
0.875	0	0.094	0.186	0.228	0	0.535	0.525	0.485	0.399	0.642
0.750	0	0.041	0.062	0.033	0	0.398	0.393	0.388	0.434	0.668
0.625	0	0.002	-0.007	-0.023	0	0.354	0.360	0.387	0.463	0.601
0.500	0	-0.013	-0.025	-0.028	0	0.365	0.375	0.408	0.469	0.539
0.375	0	-0.014	-0.023	-0.021	0	0.392	0.401	0.427	0.465	0.497
0.250	0	-0.009	-0.015	-0.012	0	0.416	0.422	0.439	0.460	0.473
0.125	0	-0.005	-0.007	-0.006	0	0.430	0.434	0.445	0.457	0.461
0	0	0	0	0	0	0.435	0.438	0.447	0.456	0.458
	σ_r/σ_3					σ_θ/σ_3				
1	0.250	0.249	0.243	0.213	-1.646	0.250	0.249	0.243	0.213	-1.646
0.875	0.548	0.565	0.629	0.797	1.000	0.548	0.555	0.581	0.647	0.828
0.750	0.782	0.802	0.865	0.957	1.000	0.782	0.792	0.825	0.888	0.977
0.625	0.921	0.932	0.961	0.990	1.000	0.921	0.928	0.949	0.982	1.018
0.500	0.985	0.988	0.995	0.999	1.000	0.985	0.988	1.018	1.011	1.022
0.375	1.008	1.007	1.005	1.001	1.000	1.008	1.009	1.012	1.015	1.017
0.250	1.013	1.011	1.007	1.002	1.000	1.013	1.013	1.013	1.013	1.011
0.125	1.012	1.011	1.006	1.002	1.000	1.012	1.012	1.011	1.008	1.007
0	1.012	1.010	1.006	1.001	1.000	1.012	1.011	1.010	1.008	1.006

TABLE C-2

$\mu = 0.4$, $\sigma_1/\sigma_3 = 0.762$, $H/D = 2$

2z/H	2r/D					2r/D				
	0	0.25	0.50	0.75	1	0	0.25	0.50	0.75	1
	$uE/D\sigma_3$					$wE/D\sigma_3$				
1	0	0	0	0	0	0	0	0	0	0
0.875	0	0.018	0.038	0.065	0.101	0.036	0.036	0.033	0.025	-0.005
0.750	0	0.030	0.063	0.098	0.132	0.047	0.046	0.040	0.027	0.008
0.625	0	0.037	0.074	0.110	0.144	0.044	0.042	0.035	0.025	0.014
0.500	0	0.039	0.077	0.114	0.149	0.034	0.033	0.028	0.021	0.016
0.375	0	0.039	0.077	0.114	0.150	0.025	0.024	0.020	0.016	0.014
0.250	0	0.039	0.077	0.114	0.150	0.016	0.015	0.013	0.011	0.010
0.125	0	0.038	0.076	0.113	0.150	0.008	0.007	0.006	0.006	0.005
0	0	0.038	0.076	0.113	0.150	0	0	0	0	0
	τ_{rz}/σ_3					σ_z/σ_3				
1	0	0.054	0.116	0.202	0.904	0.878	0.878	0.878	0.858	-3.601
0.875	0	0.042	0.082	0.100	0	0.780	0.778	0.768	0.747	0.901
0.750	0	0.016	0.023	0.009	0	0.721	0.722	0.725	0.760	0.884
0.625	0	-0.002	-0.006	-0.015	0	0.706	0.710	0.728	0.770	0.839
0.500	0	-0.008	-0.014	-0.015	0	0.714	0.719	0.738	0.769	0.803
0.375	0	-0.007	-0.012	-0.011	0	0.727	0.732	0.746	0.765	0.780
0.250	0	-0.005	-0.008	-0.006	0	0.738	0.741	0.750	0.761	0.767
0.125	0	-0.002	-0.004	-0.003	0	0.745	0.747	0.753	0.759	0.761
0	0	0	0	0	0	0.747	0.749	0.753	0.758	0.759
	σ_r/σ_3					σ_θ/σ_3				
1	0.585	0.585	0.585	0.572	-2.401	0.585	0.585	0.585	0.572	-2.401
0.875	0.755	0.764	0.799	0.886	1.000	0.755	0.760	0.780	0.826	0.961
0.750	0.883	0.893	0.926	0.973	1.000	0.883	0.890	0.912	0.954	1.007
0.625	0.957	0.963	0.976	0.993	1.000	0.957	0.962	0.976	0.999	1.024
0.500	0.992	0.993	0.997	0.999	1.000	0.992	0.994	1.001	1.010	1.019
0.375	1.004	1.004	1.003	1.001	1.000	1.004	1.005	1.008	1.011	1.012
0.250	1.007	1.007	1.004	1.001	1.000	1.007	1.008	1.008	1.008	1.007
0.125	1.008	1.007	1.004	1.001	1.000	1.008	1.008	1.007	1.006	1.005
0	1.008	1.007	1.004	1.001	1.000	1.008	1.007	1.007	1.006	1.004

TABLE C-3

$\mu = 0.45$, $\sigma_1/\sigma_3 = 0.874$, $H/D = 2$

2z/H	2r/D					2r/D				
	0	0.25	0.50	0.75	1	0	0.25	0.50	0.75	1
	$uE/D\sigma_3$					$wE/D\sigma_3$				
1	0	0	0	0	0	0	0	0	0	0
0.875	0	0.009	0.047	0.034	0.051	0.022	0.022	0.021	0.017	0.002
0.750	0	0.016	0.035	0.051	0.068	0.030	0.029	0.026	0.020	0.009
0.625	0	0.019	0.039	0.058	0.075	0.028	0.027	0.024	0.018	0.012
0.500	0	0.021	0.041	0.060	0.079	0.024	0.023	0.020	0.016	0.013
0.375	0	0.021	0.041	0.061	0.080	0.018	0.017	0.015	0.013	0.011
0.250	0	0.021	0.041	0.061	0.081	0.011	0.011	0.010	0.009	0.008
0.125	0	0.021	0.041	0.061	0.081	0.005	0.005	0.004	0.004	0.004
0	0	0.021	0.041	0.061	0.081	0	0	0	0	0
	τ_{rz}/σ_3					σ_z/σ_3				
1	0	0.028	0.060	0.104	0.460	0.934	0.935	0.937	0.932	-2.771
0.875	0	0.021	0.042	0.051	0	0.885	0.885	0.883	0.879	0.963
0.750	0	0.008	0.012	0.006	0	0.855	0.857	0.861	0.880	0.946
0.625	0	0	-0.003	-0.007	0	0.847	0.849	0.859	0.881	0.919
0.500	0	-0.003	-0.007	-0.007	0	0.848	0.851	0.861	0.878	0.897
0.375	0	-0.004	-0.006	-0.006	0	0.853	0.856	0.863	0.874	0.883
0.250	0	-0.002	-0.004	-0.003	0	0.857	0.859	0.864	0.870	0.875
0.125	0	-0.001	-0.002	-0.002	0	0.860	0.861	0.864	0.868	0.870
0	0	0	0	0	0	0.861	0.862	0.865	0.868	0.869
	σ_r/σ_3					σ_θ/σ_3				
1	0.765	0.765	0.767	0.763	-2.267	0.765	0.765	0.767	0.763	-2.267
0.875	0.860	0.865	0.884	0.930	1.000	0.860	0.863	0.875	0.904	0.986
0.750	0.931	0.937	0.954	0.981	1.000	0.931	0.935	0.948	0.973	1.012
0.625	0.973	0.976	0.985	0.995	1.000	0.973	0.976	0.985	0.998	1.014
0.500	0.994	0.995	0.997	0.999	1.000	0.994	0.995	1.000	1.006	1.011
0.375	1.002	1.002	1.002	1.001	1.000	1.002	1.003	1.007	1.007	1.008
0.250	1.005	1.005	1.003	1.001	1.000	1.005	1.005	1.006	1.006	1.005
0.125	1.006	1.005	1.004	1.002	1.000	1.006	1.006	1.005	1.005	1.004
0	1.006	1.005	1.004	1.002	1.000	1.006	1.006	1.005	1.004	1.003

Some Implications of Viscoelastic Subgrade Behavior

B. B. SCHIMMING, Assistant Professor, Department of Civil Engineering, University of Notre Dame; and
J. VALERA, Research Assistant, Department of Civil Engineering, University of California, Berkeley

The two-dimensional viscoelastic displacement equations for a Voigt solid are approached on a numerical basis to examine the effect of viscosity on the load-settlement-time relation in an ideal soil. Curves indicating the viscosity effect on surface settlement and displacement within the soil mass as a function of time for an applied surface load are presented. In addition, the generality of the method for approaching mixed boundary conditions is demonstrated by the determination of heave in the bottom of an excavation due to an applied surface load.

•THE PROBLEM of determining the stresses and displacements within a homogeneous soil mass due to an imposed surface load has been extensively treated in the literature. It is usually assumed in problems of this type that the deformations and stresses developed within the soil can be computed on the basis of the classical theory of elasticity which assumes that a linear relation exists between stress and strain and that strains are small. The basic solution of this problem is the well-known Boussinesq solution for a single, vertical point load acting on the horizontal surface of a semi-infinite, homogeneous, isotropic elastic solid (1). This solution has been extended to include various surface load configurations by a number of investigators (2, 3, 4, 5, 6, 7, 8). Their results have been useful and of proven practical value.

However, the presence of viscous effects in the mechanical behavior of soil raises a question regarding the influence of this effect on the resulting stress analysis. Instead of being considered elastic, the foundation may, therefore, be more closely approximated by a viscoelastic medium. This problem differs from the corresponding elastic problem, since time appears in the stress-strain relations and, hence, the boundary conditions and the solution must involve the history of the process throughout the time range of interest. The variation of the displacements and the stress distribution with time is sought, and it is found that, in general, the history of loading has a marked influence. This is in contrast to the corresponding elastic problem for which the displacements and stress distribution are functions only of the instantaneous values of the surface displacements and stresses, and not of the loading history (9).

The two elements whose combination represents linear viscoelastic behavior are the linearly elastic spring and the viscous dashpot filled with a Newtonian liquid. The motion of the piston inside the dashpot produces a resisting force in the liquid which is proportional to the velocity of the piston. Figure 1 shows combinations of these elements which form the simplest linear viscoelastic models. If a soil mass is represented as a Voigt material, the displacements will eventually approach the elastic values, whereas with a Maxwell representation, the initial displacements will equal the elastic displacements. Thus, a Voigt solid is of interest with regard to short-term departures from classical elasticity, whereas a Maxwell material relates to long-term departures. More sophisticated models may be constructed by different combinations of the two original elements (10, 11, 12, 13, 14).
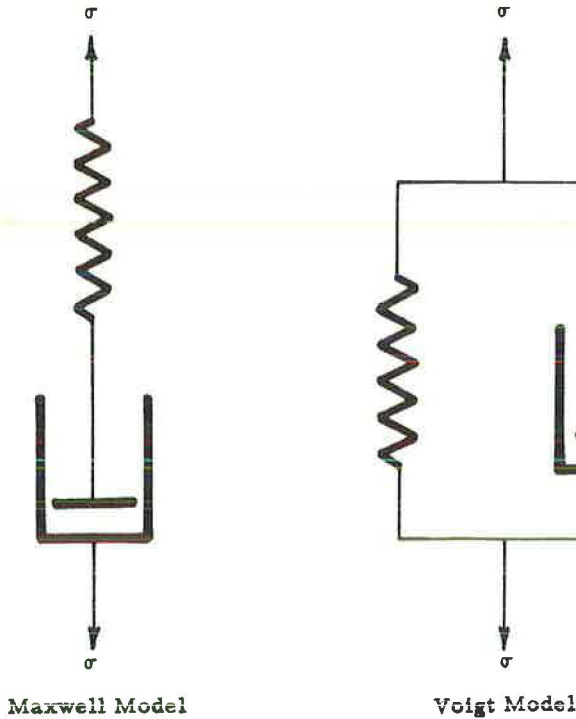

Figure 1. Typical viscoelastic models.

In recent years it has been shown that under certain circumstances the stress analysis of a system including linear viscoelastic components can be treated in terms of the analogous elastic problem having the same geometry and boundary conditions. In the case of a system, for which the geometry does not change and the boundary conditions remain of the same type during the loading process, application of the Laplace transform removes the time dependence and transforms the problem into an associated elastic problem. Thus, the determination of transformed variables, e.g., of stress or displacement, becomes an elasticity problem and standard methods of inversion of the Laplace transform determine the stresses and displacements as a function of time. Hoskin and Lee (15) and Lee (16) have determined stress as a function of time for a viscoelastic Maxwell foundation acted on by a uniformly loaded elastic plate. Pister (17) obtained a solution to the same problem where the plate was also viscoelastic. In all these cases, Laplace transforms were employed, so that it was first necessary to know the elastic solution to the problem before the viscoelastic solution could be found. If the elastic solution is unknown, the solution to the corresponding viscoelastic problem cannot be obtained with this approach.

In view of this situation, a desirable alternative would be to approach the viscoelastic problem directly on a numerical basis, thus eliminating the requirement of an elastic solution which may not be available for a particular foundation problem.

The ultimate objective of this presentation is to examine the effect of the Voigt solid viscosity parameters on the short-term displacements of a soil mass subjected to boundary forces. Of particular interest is the development of lateral strains beneath a uniform surface load as a function of time which gives rise to displacements of the type schematically indicated in Figure 2. The importance of this effect has been recently described by Lambe (18).
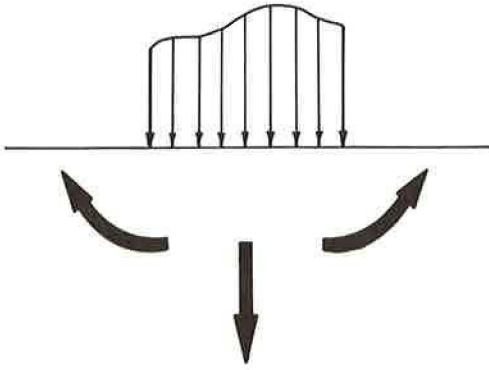
Figure 2. Schematic representation of displacements.

$$\sigma_{zz} = \lambda(\epsilon_{zz} + \epsilon_{yy}^{0} + \epsilon_{xx}^{0}) + 2\mu\epsilon_{zz}$$

$$\sigma_{zz} = (\lambda + 2\mu)\epsilon_{zz}$$

Figure 3. One-dimensional stress strain.

DESCRIPTION OF VOIGT SOLID

The development of the two-dimensional field equations for a soil requires a description of both the dilatational and distortional components of behavior. The inability of the conventional one-dimensional test to provide this description is demonstrated with respect to the consolidation test in Figure 3. Even if the soil is considered to be elastic and the appropriate stress-strain relations are written in terms of Lame's constants, the resulting response involves both volume change and shear, thus disallowing their individual determination. Any realistic viscoelastic description of a soil will eventually necessitate the development of appropriate laboratory tests for the determination of the fundamental mechanical constants involved.

The following development is most conveniently accomplished by formulating the elastic equation and then converting to the viscoelastic condition. In the absence of an exact stress-strain-time relation, a Voigt solid which is known to be similar to soil in some respects was assumed.

The relationships between stress and strain for a homogeneous, isotropic elastic solid may be written as:

$$\sigma_{xx} = \lambda\Delta + 2\mu\epsilon_{xx}, \quad \sigma_{yy} = \lambda\Delta +$$
$$2\mu\epsilon_{yy}, \quad \sigma_{zz} = \lambda\Delta + 2\mu\epsilon_{zz},$$
$$\tau_{yz} = \mu\epsilon_{yz}, \quad \tau_{zx} = \mu\epsilon_{zx},$$
$$\tau_{xy} = \mu\epsilon_{xy} \quad (1)$$

where

Lame's coefficient $\lambda = \dfrac{E\nu}{(1 + \nu)(1 - 2\nu)}$,

Lame's coefficient $\mu = \dfrac{E}{2(1 + \nu)}$, and

$$\Delta = \epsilon_{xx} + \epsilon_{yy} + \epsilon_{zz} = \frac{\partial u}{\partial x} + \frac{\partial v}{\partial y} + \frac{\partial w}{\partial z}.$$

Substitution of the stress-strain relationships into the equilibrium equations in the x-y plane yields in the absence of body forces:

$$(\lambda + 2\mu) \frac{\partial^2 u}{\partial x^2} + \mu \frac{\partial^2 u}{\partial y^2} + (\lambda + \mu) \frac{\partial^2 v}{\partial x \partial y} + \lambda \frac{\partial^2 w}{\partial x \partial z} = 0 \tag{2}$$

and

$$\mu \frac{\partial^2 v}{\partial x^2} + (\lambda + 2\mu) \frac{\partial^2 v}{\partial y^2} + (\lambda + \mu) \frac{\partial^2 u}{\partial x \partial y} + \frac{\partial^2 w}{\partial y \partial z} = 0 \tag{3}$$

where u, v and w are the displacements in the x, y and z directions, respectively.

For a condition of plane strain $\frac{\partial w}{\partial z} = 0$. Eqs. 2 and 3 reduce to:

$$(\lambda + 2\mu) \frac{\partial^2 u}{\partial x^2} + \mu \frac{\partial^2 u}{\partial y^2} + (\lambda + \mu) \frac{\partial^2 v}{\partial x \partial y} = 0 \tag{4}$$

and

$$\mu \frac{\partial^2 v}{\partial x^2} + (\lambda + 2\mu) \frac{\partial^2 v}{\partial y^2} + (\lambda + \mu) \frac{\partial^2 u}{\partial x \partial y} = 0 \tag{5}$$

Eqs. 4 and 5 can be modified to express the behavior of a Voigt solid by an appropriate change of coefficients (19). Substitution of $\lambda + \lambda' \frac{\partial}{\partial t}$ for λ and $\mu + \mu' \frac{\partial}{\partial t}$ for μ into Eq. 4 yields:

$$\left[\lambda + \lambda' \frac{\partial}{\partial t} + 2 \left(\mu + \mu' \frac{\partial}{\partial t} \right) \right] \frac{\partial^2 u}{\partial x^2} + \left(\mu + \mu' \frac{\partial}{\partial t} \right) \frac{\partial^2 u}{\partial y^2} + \left(\lambda + \lambda' \frac{\partial}{\partial t} + \right.$$
$$\left. \mu + \mu' \frac{\partial}{\partial t} \right) \frac{\partial^2 v}{\partial x \partial y} = 0 \tag{6}$$

where λ' and μ' are the viscosity coefficients corresponding to the Lame coefficients. On rearranging terms, Eq. 6 becomes:

$$(\lambda + 2\mu) \frac{\partial^2 u}{\partial x^2} + (\lambda' + 2\mu') \frac{\partial}{\partial t} \left(\frac{\partial^2 u}{\partial x^2} \right) + \mu \frac{\partial^2 u}{\partial y^2} + \mu' \frac{\partial}{\partial t} \left(\frac{\partial^2 u}{\partial y^2} \right) +$$
$$(\lambda + \mu) \frac{\partial^2 v}{\partial x \partial y} + (\lambda' + \mu') \frac{\partial}{\partial t} \left(\frac{\partial^2 v}{\partial x \partial y} \right) = 0 \tag{7}$$

Proceeding in the same manner for Eq. 5, Eq. 8 is obtained:

$$\mu \frac{\partial^2 v}{\partial x^2} + \mu' \frac{\partial}{\partial t} \left(\frac{\partial^2 v}{\partial x^2} \right) + (\lambda + 2\mu) \frac{\partial^2 v}{\partial y^2} + (\lambda' + 2\mu') \frac{\partial}{\partial t} \left(\frac{\partial^2 v}{\partial y^2} \right) +$$
$$(\lambda + \mu) \frac{\partial^2 u}{\partial x \partial y} + (\lambda' + \mu') \frac{\partial}{\partial t} \left(\frac{\partial^2 u}{\partial x \partial y} \right) = 0 \tag{8}$$

Eqs. 7 and 8 are the equations of equilibrium in terms of displacements for a two-dimensional linear viscoelastic Voigt medium for the particular case where a plane strain condition exists.

Eqs. 7 and 8 can now be reduced to finite difference form. A typical difference approximation to Eq. 7 along with the grid notation is given in Figure 4. By this tech-
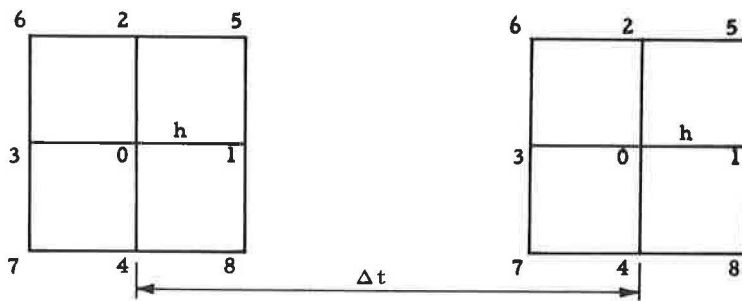
$$A_1 (u_3 - 2u_0 + u_1)_{t_0 + \Delta t} + B_1 (u_2 - 2u_0 + u_4)_{t_0 + \Delta t}$$

$$+ A_2 (v_5 - v_6 + v_7 - v_8)_{t_0 + \Delta t} = A_3 (u_3 - 2u_0 + u_1)_{t_0}$$

$$+ B_2 (u_2 - 2u_0 + u_4)_{t_0} + A_4 (v_5 - v_6 + v_7 - v_8)_{t_0}$$

where

$$A_1 = (\lambda \Delta t + 2\mu \Delta t + 2\lambda' + 4\mu')$$

$$A_3 = (-\lambda \Delta t - 2\mu \Delta t + 2\lambda' + 4\mu')$$

$$A_2 = 1/4 (\lambda \Delta t + \mu \Delta t + 2\lambda' + 2\mu')$$

$$A_4 = 1/4 (-\lambda \Delta t - \mu \Delta t + 2\lambda' + 2\mu')$$

$$B_1 = \mu \Delta t + 2\mu' \qquad B_2 = -\mu \Delta t + 2\mu'$$

Figure 4. Finite difference approximation.
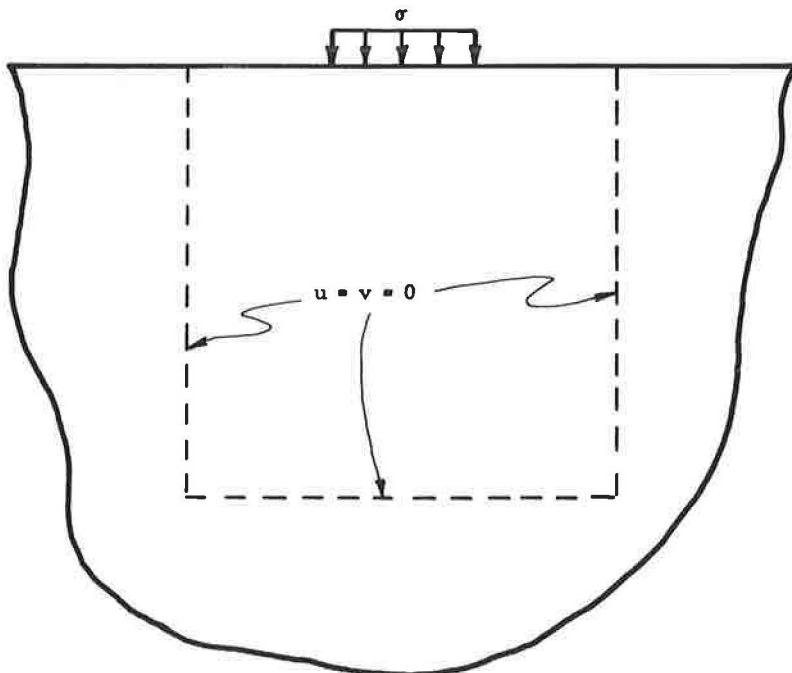
Figure 5. Statement of boundary conditions.

nique, the governing partial differential equations that are often impossible to solve in closed form can be transformed into a set of linear simultaneous algebraic equations. This transformation involves expressing the pertinent equations in terms of values of the desired function at finite points in the system under analysis. By utilizing a digital computer, the resulting equations can then be solved by a matching procedure with respect to the independent time variable.

For the particular case of a uniform surface load, the dependent displacement variables must be defined on the boundary of the region beneath the load which requires an approximation in the case of a numerical approach to a half space. Thus, the displacements were set equal to zero along the dashed lines in Figure 5. The effect of this assumption will be subsequently discussed.

DISPLACEMENT RESULTS

Figure 6 is a graph of the displacement of the surface at the centerline of the load vs the logarithm of time for various values of the viscosity coefficients. It is of interest to note the significant role played by μ' which is equivalent to a shear viscosity. The largest value of $\mu' = 5,000 \times E$ displays the most retarded displacement. This effect is considerably larger than the role played by λ'. Thus, for the configuration of this problem, the resistance to lateral strains beneath the applied load as dictated by a
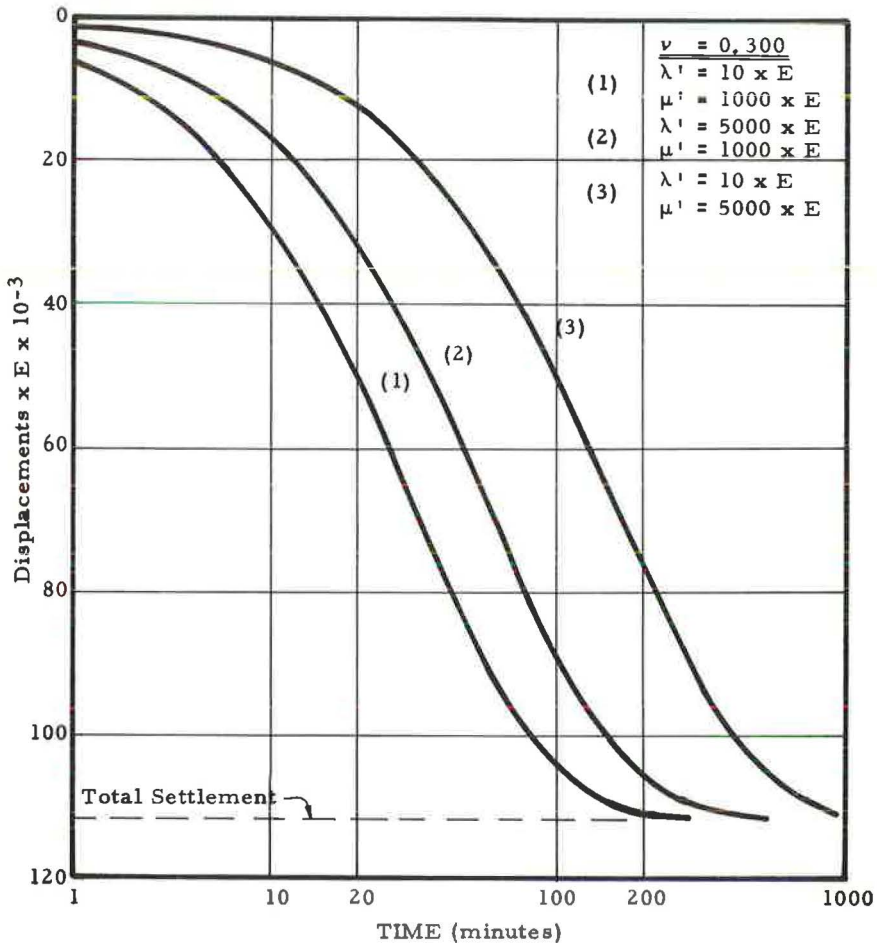
Figure 6. Vertical displacement at centerline of load.

large shear viscosity can significantly alter the deflection time relationship. The ultimate settlement is, of course, independent of the viscosity coefficient for a Voigt material, depending only on the elastic constants which are the same for all the cases in Figure 6.

Figures 7 and 8 present vertical displacements as a function of depth and time. Again, the shear viscosity effect is graphically displayed. In Figure 7, which involves the smaller shear viscosity, an actual heave or bulge initially occurs adjacent to the applied load. Gradually, as volume change takes place, the top surface subsides, removing the heave until the elastic equilibrium position is reached.
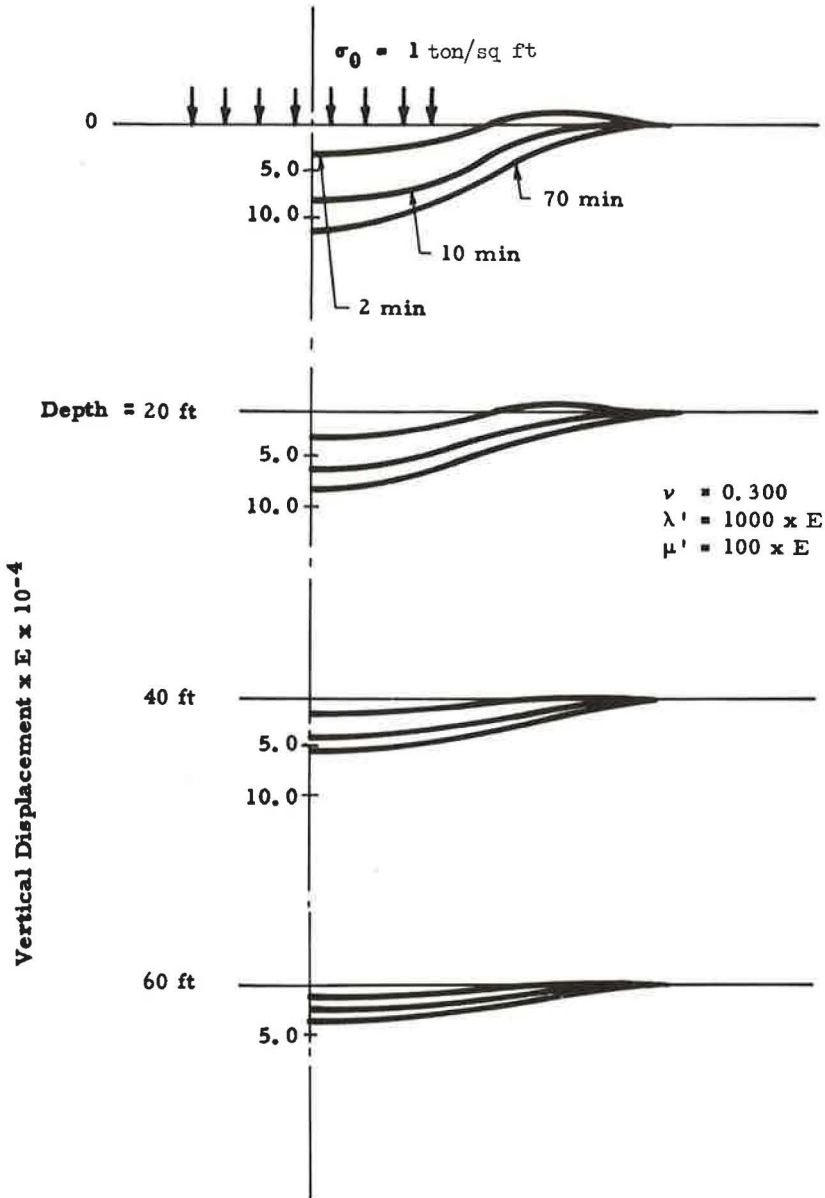
Figure 7. Vertical displacement as function of depth and time.
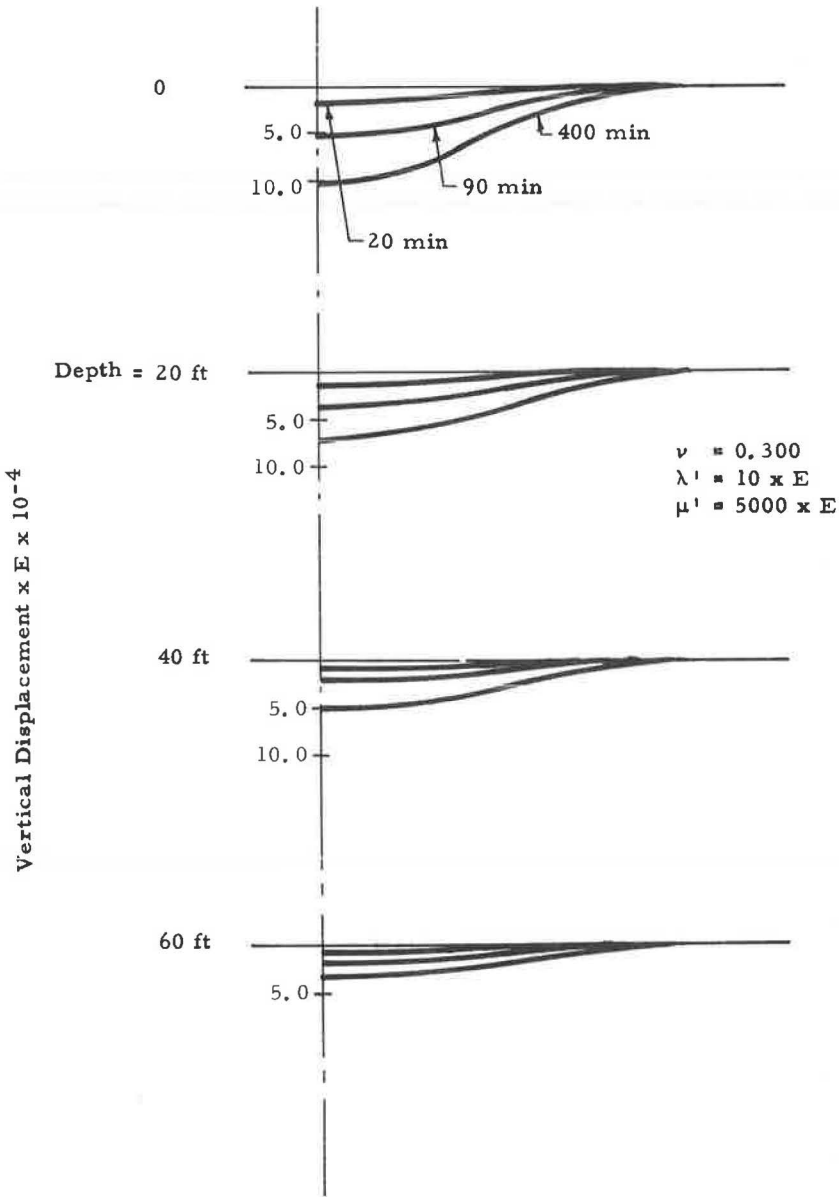
Figure 8. Vertical displacement as function of depth and time.

In contrast, a large shear viscosity, as indicated in Figure 8, shows no initial heave at the surface. This essentially means that the development of lateral strains is retarded which, in turn, retards the surface displacement. This is, of course, consistent with the settlement time plots in Figure 6.

To examine the boundary effect assumption, the vertical stresses at two different depths are compared in Figure 9. One distribution is the elastic case as presented by Jurgenson (20), and the other is the final viscoelastic value. The agreement appears to be acceptable in view of the numerical approximation involved. In addition, the motivation for the study was not to develop quantitatively a specific solution, but also to examine in a qualitative manner the effect of the time-dependent viscoelastic parameters on the form of the solution.

Depth = 20 ft

$0.5\sigma_0$

Elastic Solution

Final Numerical Viscoelastic
Solution

Depth = 60 ft

Elastic Solution

$0.5\sigma_0$

Final Numerical Viscoelastic
Solution
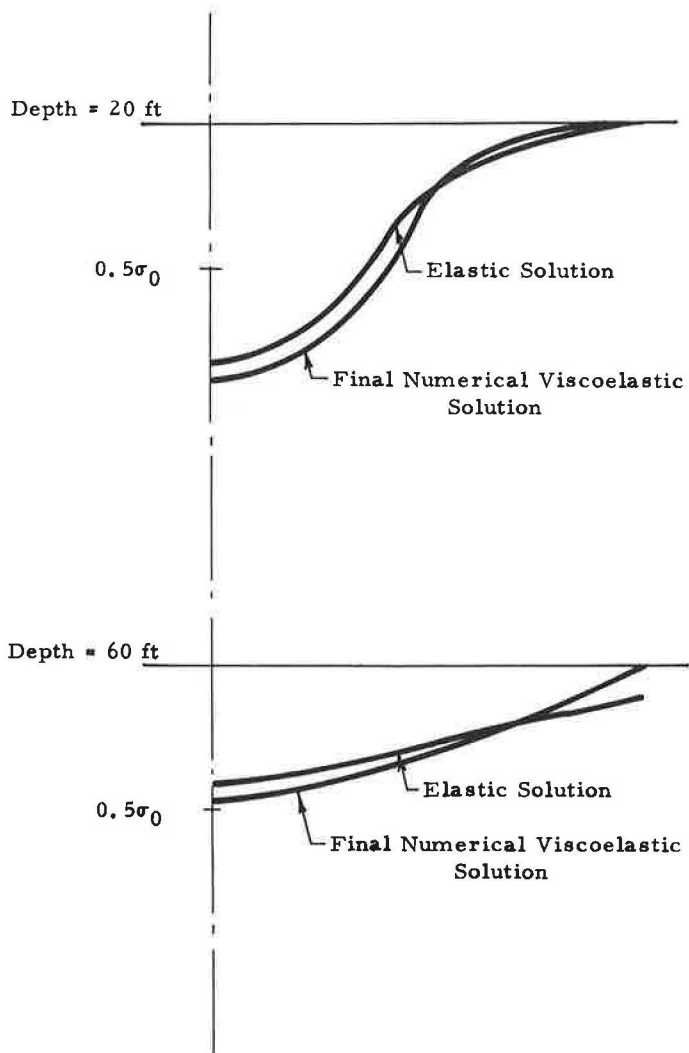
Figure 9.   Vertical Stress distribution.

$u = v = 0$

$u = v = 0$
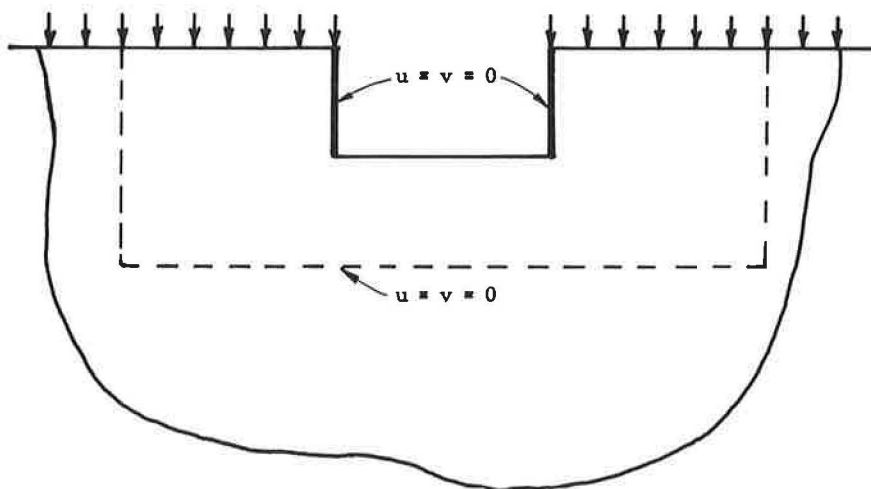
Figure 10.   Description of excavation problem.
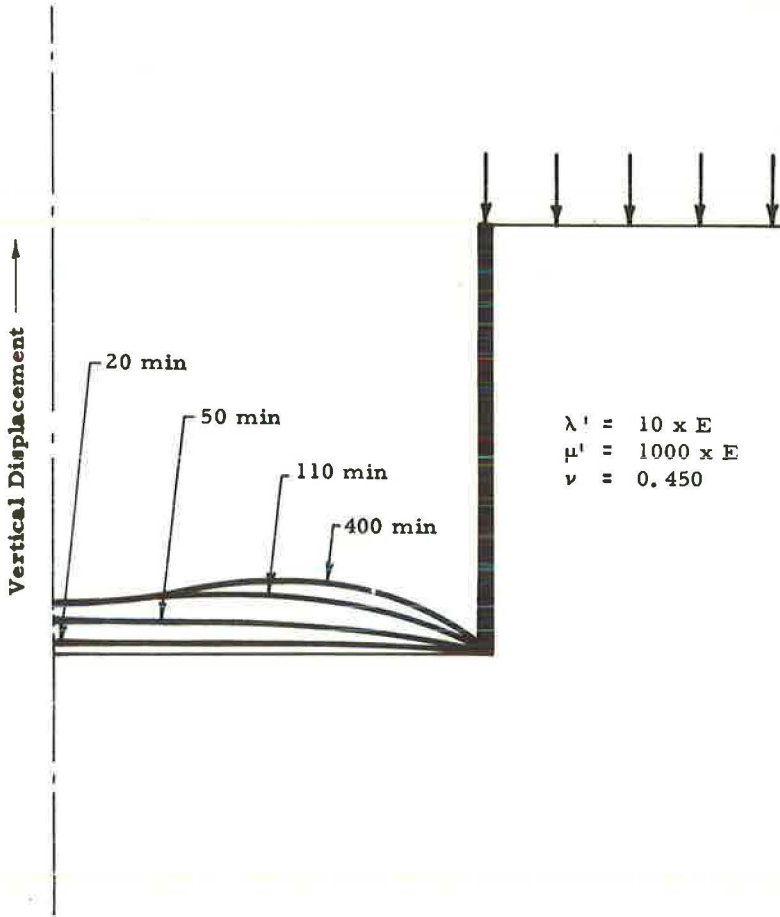
Figure 11. Displacements at bottom of excavation.

A final comment regarding the flexibility of the numerical procedure employed can be made with reference to Figure 10. The upward displacement of the bottom of an excavation due to the application of a uniform load at the surface is desired. The sides of the excavation are assumed to be fixed against any movement (u = v = 0).

The resulting heave at the bottom of the cut as a function of time is shown in Figure 11. The particular shape of these curves is, of course, a function of the geometry of the excavation. A very wide excavation with respect to depth would probably exhibit very little heave at the centerline.

CONCLUSIONS

A particular viscoelastic material, a Voigt solid, was chosen to represent the behavior of a soil for the purpose of analyzing the effect of viscoelastic behavior on certain common foundation situations. No illusion is entertained regarding the adequacy of a Voigt solid. A more complete equation of state is, of course, required. However, the importance of considering not only the time-dependent volume change characteristics of soil but also the time-dependent distortional properties has been qualitatively demonstrated. A one-dimensional theory cannot be expected to describe the time-dependent settlement of isolated surface loads located on deep layers of soil.

REFERENCES

1. Boussinesq, J. Application des Potentiels a l'Etude de l'Equilibre et du Mouvement des Solides Elastiques. Paris, Gauthier-Villars, 1885.
2. Love, A. E. H. The Stress Produced in a Semi-Infinite Body by Pressure on Part of the Boundary. Phil. Trans., Royal Soc. (London), Series A, Vol. 228, pp. 377-420, 1928.
3. Newmark, N. M. Influence Charts for Computation of Stresses in Elastic Foundations. Univ. of Illinois, Eng. Exp. Sta., Bull. No. 338, 1942.
4. Newmark, N. M. Influence Charts for Computation of Vertical Displacements in Elastic Foundations. Univ. of Illinois, Eng. Exp. Sta., Bull. No. 367, 1947.
5. Pickett, G. Stress Distribution in a Loaded Soil With Some Rigid Boundaries. Highway Research Board Proc. Vol. 18, Pt. 2, pp. 35-48, 1938.
6. Schiffman, R. L. Stresses and Displacements Produced in a Semi-Infinite Elastic Solid by a Rigid Elliptical Footing. Proc. 5th Int. Conf. on Soil Mech. and Found. Eng., Vol. 1, pp. 795-801, 1961.
7. Fergus, S. M., and Miner, W. E. Distributed Loads on Elastic Foundations: The Uniform Circular Load. Highway Research Board Proc., Vol. 34, pp. 582-597, 1955.
8. Koning, H. Stress Distribution in a Homogeneous, Anisotropic, Elastic Semi-Infinite Solid. Proc. 4th Int. Conf. on Soil Mech. and Found. Eng., Vol. 1, pp. 335-338, 1957.
9. Bergen, J. T. Viscoelasticity. P. 1. New York, Academic Press, 1960.
10. Burgers, J. M. Phenomenological Theories of Relaxation and Viscosity. 1st Rept. on Viscosity and Plasticity, Holland, pp. 5-72, 1939.
11. Bland, D. R. The Theory of Linear Viscoelasticity. Pergamon Press, 1960.
12. Schiffman, R. L. The Use of Visco-Elastic Stress-Strain Laws in Soil Testing. ASTM Spec. Tech. Pub. No. 254, pp. 131-155, 1957.
13. Reiner, M. Deformation, Strain and Flow. New York Interscience Publishers, 1960.
14. Saada, A. S. A Rheological Analysis of Shear and Consolidation of Saturated Clays. Highway Research Board Bull. 342, pp. 52-89, 1962.
15. Hoskin, B. C., and Lee, E. H. Flexible Surfaces on Viscoelastic Subgrades. Trans. ASCE, Vol. 126, Pt. 1, pp. 1714-1733, 1961.
16. Lee, E. H. Stress Analysis for Viscoelastic Bodies. In Viscoelasticity, pp. 1-25. New York, Academic Press, 1960.
17. Pister, K. S. Viscoelastic Plate on a Viscoelastic Foundation. Jour. Eng. Mech. Div., ASCE, Vol. 87, No. 1, pp. 43-54, Feb. 1961.
18. Lambe, E. W. Methods of Estimating Settlement. ASCE Settlement Conf., June 1964.
19. Kolsky, H. Stress Waves in Solids. P. 108. Dover Publications, 1963.
20. Jurgenson, L. The Application of Theories of Elasticity and Plasticity to Foundation Problems. Contrib. to Soil Mech., Boston Soc. of Civil Eng., p. 148, July 1934.

Void Ratio Effects on Lateral Stability of Rigid Poles Partially Embedded in Sands

ROBERT L. KONDNER, PAUL PFISTER and JOSEPH S. ZELASKO
Northwestern University

An investigation was made of the effects of void ratio on the lateral stability of rigid poles partially embedded in a saturated sand and subjected to a horizontal load applied a vertical distance, D, above the groundline. Void ratio effects are presented in terms of the dimensionless parameter, relative density. Nondimensional techniques in conjunction with small-scale model studies are used to determine the interrelationship among the physical variables. Tests were conducted in a quicksand tank device to control relative density. A response equation is given from which the load-deflection characteristics of a prototype pole might be estimated. The results have been compared with previous studies and satisfactory agreement was obtained. Explicit equations are given for certain circular poles, and expressions are developed for the ultimate value of the moment parameter and for the initial tangent modulus of the moment-deflection relation.

•NONDIMENSIONAL TECHNIQUES and small-scale model experiments are used to study the effect of relative density on the response of laterally loaded poles partially embedded in a cohesionless soil. A pole is considered a partially embedded rigid member whose deflections under load are primarily due to rigid body motions. Such poles are utilized in construction as anchorages, as well as by utilities, railroads, highway departments, etc. Failure of a pole is assumed to mean failure of the soil with excessive rotation of the pole since a proper structural design will avoid flexural failure of the pole itself. Because of the difficulty of associating the relative density to the elastic or elasto-plastic properties of a cohesionless soil, the problem is considered in terms of the physical variables involved using dimensional analysis. Although dimensional analysis in conjunction with small-scale model tests has not been extensively used in soil mechanics, there are instances of such studies (<u>1</u>, <u>2</u>, <u>3</u>). The present study is an extension of the work of Kondner et al. (<u>2</u>, <u>3</u>).

THEORETICAL ANALYSIS

The general methods of dimensional analysis and the particular situations encountered in the field of soil mechanics when applying this tool have been previously described in detail by Kondner and Green (<u>2</u>) and are not discussed again here. The physical quantities considered are given in Table 1 in terms of a force-length-time system of fundamental units. Since there are twelve physical quantities and three fundamental units, there must be nine independent, nondimensional π terms. There is nothing unique about the form of the π terms and it is possible to transform them algebraically as long as the final π terms are nondimensional and independent.

The following nondimensional independent π terms were derived:

$$\pi_1' = \frac{X}{C}, \quad \pi_2' = \frac{M}{\gamma_d C^2 L^2}, \quad \pi_3' = \frac{C}{L}, \quad \pi_4' = \frac{D}{L}, \quad \pi_5' = \frac{C^2}{A},$$

$$\pi_6' = \phi, \quad \pi_7' = \frac{\gamma_d t C}{\eta}, \quad \pi_8' = D_r, \quad \pi_9' = \theta \tag{1}$$

TABLE 1

PHYSICAL QUANTITIES CONSIDERED IN DIMENSIONAL
ANALYSIS OF RIGID POLE EMBEDDED IN SAND

Physical Quantity	Symbol	Fundamental Units
Horizontal deflection at groundline	X	L
Depth of embedment	L	L
Cross-sectional area of pole	A	L^2
Perimeter of pole	C	L
Moment arm (distance from ground-line to point of load application)	D	L
Moment at groundline (product of load times moment arm)	M	FL
Dry density of sand	γ_d	FL^{-3}
Angle of internal friction	ϕ	$F°L°T°$
Viscosity of sand	η	$FL^{-2}T$
Time of loading	t	T
Relative density	D_r	$F°L°T°$
Rotation of pole	θ	$F°L°T°$

Since the effect of variable density was the primary purpose of this study, and to avoid keeping too many terms in the final relationship, the π_2' term was transformed into:

$$\pi_2 = \frac{M}{\gamma_d C^2 L^2} \times \frac{1}{1 + 2D_r} = \frac{M}{\gamma_d C^2 L^2 (1 + 2D_r)} \qquad (2)$$

and π_8' became:

$$\pi_8'' = (1 + 2D_r) \qquad (3)$$

and

$$\pi_8 = \frac{1 + 2D_r}{1 + 2D_r} = 1 \qquad (4)$$

The term $(1 + 2D_r)$ was found, by experiment, to group the load-deflection curves for any series of tests in which only the density was varied into essentially one curve. This is shown by Figures 1 and 2. Figure 1 shows the dimensionless plots of $M/\gamma_d C^2 L^2$ vs X/C for three representative tests, the only difference being the relative density. Figure 2 indicates the applicability of the term $(1 + 2D_r)$ to collapse these curves. The variable γ_d is not a constant value for the three tests; however, its changes in magnitude are minor and are included in the final response formulation. Thus, the final set of π terms used for this study was:

$$\pi_1 = \frac{X}{C}, \quad \pi_2 = \frac{M}{\gamma_d C^2 L^2 (1 + 2D_r)}, \quad \pi_3 = \frac{C}{L}, \quad \pi_4 = \frac{D}{L},$$

$$\pi_5 = \frac{C^2}{A}, \quad \pi_6 = \phi, \quad \pi_7 = \frac{\gamma_d t C}{\eta}, \quad \pi_9 = \theta \qquad (5)$$

The functional relationship developed using dimensional analysis has been written as:
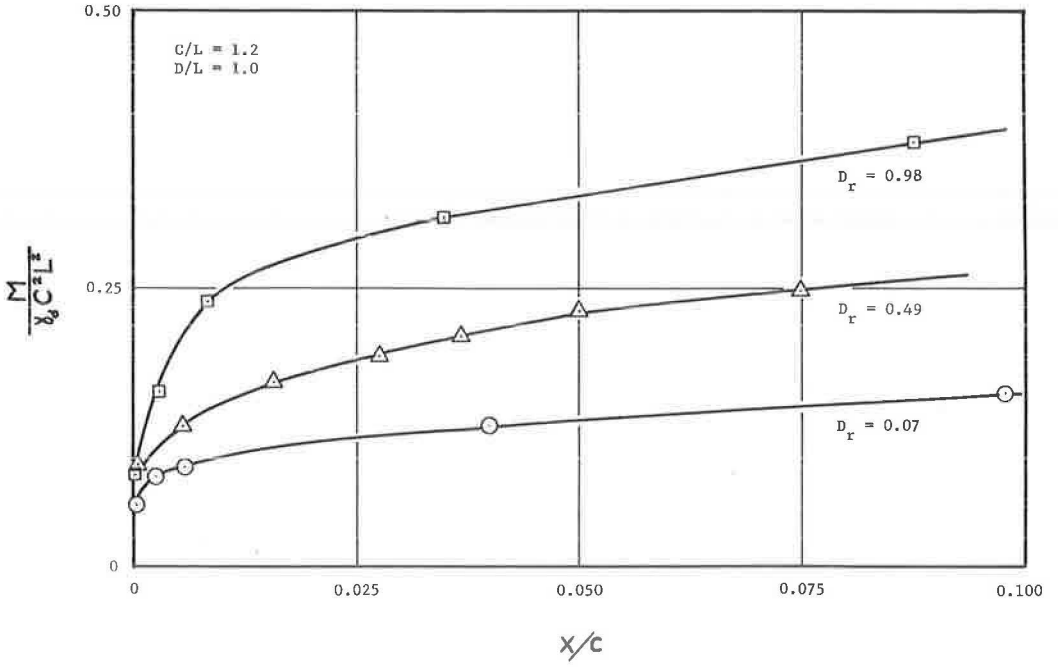
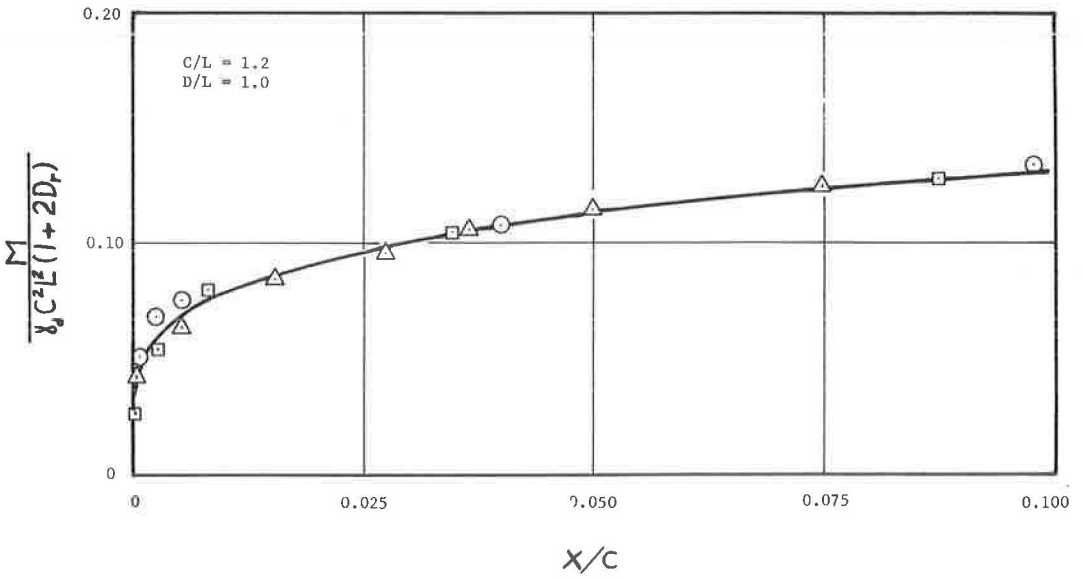Figure 1. Preliminary form of moment-strength parameter vs X/C for various values of D_r.

Figure 2. Final form of moment-strength parameter vs X/C for various values of D_r.

$$\frac{X}{C} = \varkappa \left[\frac{M}{\gamma_d C^2 L^2 (1 + 2D_r)}, \quad \frac{C}{L}, \quad \frac{D}{L}, \quad \frac{C^2}{A}, \quad \phi, \quad \frac{\gamma_d t C}{\eta}, \quad \theta \right] \tag{6}$$

The dependent variable is X/C, called a deflection ratio. Shape effects are included in the shape factor term C^2/A. By limiting the study to circular cross-sections, the value of C^2/A is a constant equal to 4π regardless of the size. The perimeter C is not necessarily the best choice of variable when dealing with irregular shapes, but this study is limited to circular poles. Additional work is needed to determine the most generally applicable form of this variable. The parameter D/L is a relative measure of moment arm to the embedment and is called the embedment ratio. The slenderness ratio is the term C/L. The parameter $M/\gamma_d C^2 L^2(1 + 2D_r)$, the moment-strength ratio, is the ratio of the applied moment to some form of strength parameter of the soil-pole system. The term $\gamma_d t C/\eta$ includes time effects; however, by proper choice of the loading rate, its effect can be minimized. For the present study, the rotation θ can be expressed in terms of the other geometric variables. A single sand was used in this study and variations in the angle of internal friction due to variations in void ratio were assumed to be accounted for in terms of the relative density. Thus, by restricting the problem to consideration of circular poles embedded in a particular sand and subjected to a proper load-time program, it is possible to simplify the functional relationship of Eq. 6 to the form:

$$\frac{X}{C} = \varkappa \left[\frac{M}{\gamma_d C^2 L^2(1 + 2D_r)}, \quad \frac{C}{L}, \quad \frac{D}{L} \right] \tag{7}$$

EXPERIMENTAL PROCEDURE

Sand

The particular sand used was a medium to fine clean beach sand with a specific gravity of 2.70 and a gradation curve as shown in Figure 3. For its densest state, i.e., $D_r = 1.0$, its dry density was 108 pcf, and in its loosest state, i.e., $D_r = 0.0$, dry density was 96 pcf. Most experiments (an experiment being defined by a value of the embedment ratio D/L and a value of the slenderness ratio C/L) were run for relative densities of 1.0, 0.5 and 0.0, successively. Some tests were conducted for other values of D_r to check the validity of the moment-strength ratio parameter used for this study.

Model Poles

The model poles consisted of various lengths of polished aluminum or steel tube plugged at the lower ends. The properties of these poles are given in Table 2.

TABLE 2

PROPERTIES OF MODEL POLES

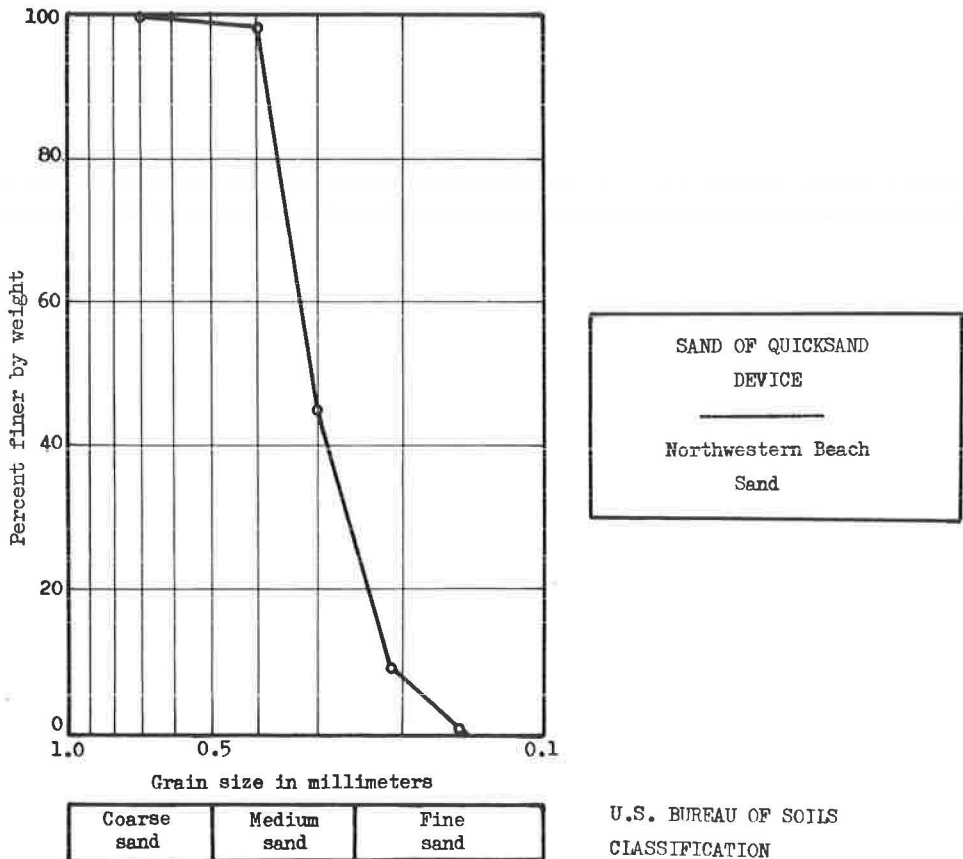| Pole No.	Material	Diameter		Area		Wt. (gm)	Perimeter	
		In.	Cm	Sq In.	Sq Cm		In.	Cm
1	Aluminum	0.501	1.273	0.197	1.263	30	1.573	3.996
2	Aluminum	0.626	1.590	0.307	1.981	62	1.966	4.993
3	Steel	0.707	1.796	0.393	2.535	143	2.221	5.641
4	Steel	0.927	2.355	0.674	4.349	216	2.911	7.394
5	Steel	1.248	3.170	1.222	7.819	229	3.921	9.959
6	Steel	1.515	3.848	1.801	11.619	478	4.755	12.077

Figure 3.   Grain size distribution of sand.

Apparatus

Because of the difficulty of obtaining a reasonable distribution of uniform interme-diate values of void ratio (relative density) by compaction and vibratory methods, the so-called quicksand tank developed for quicksand and seepage experiments was used. This apparatus, a schematic diagram of which is shown in Figure 4, proved to be ex-tremely convenient for the pole experiments. Water flowing upward at a controlled rate through the sand loosens it to its minimum density. To obtain any denser state of the sand, the tank walls were tapped with a rubber mallet so that the sand was den-sified by the applied shocks. Good reproducibility was obtained by this technique.

The tank contained 394 lb of oven-dried sand and the volume (hence, relative den-sity) was determined from a previously obtained calibration curve by reading the height of the sand on scales placed at the four corners of the tank and averaging the readings. The load was applied to the model pole by hanging weights on a cord attached to the pole and passing over three small pulleys, as shown in Figure 4. Frictional forces in the apparatus were minimized and the internal springs in the indicator dials were re-moved. The sand was always in a saturated state with the level of the water slightly above the sand level.

TABLE 3

TESTS PERFORMED

C/L	D/L	D_r			Other
		1.0	0.5	0.0	
0.4	0.2	xx	x	x	
	0.4	xx	x	x	x
	0.6	xx	xx	xxx	
	0.8	xxx	xx	xx	
	1.0	xx	xxx	x	
	1.2	xx	xxx	x	
0.6	0.2	x		x	x
	0.4	x		x	
	0.6	x		x	x
	0.8	x		x	x
	1.0	x		x	x
	1.2	x		x	x
0.8	0.2	x	x	x	
	0.4	x	xx	x	
	0.6	x	x	x	
	0.8	xx	xx	x	x
	1.0	x	x	x	
	1.2	x	xx	x	
1.0	0.2	x	x	x	x
	0.4	xx	x	xx	
	0.6	x	x	x	
	0.8	x	x	x	
	1.0	x	x	xx	
	1.2	xx	x	xx	
1.2	0.2	x	x	x	xx
	0.4	x	x	x	
	0.6	x	x	x	x
	0.8	xx	xx	x	
	1.0	xx	x	x	
	1.2	xx	xx	xx	
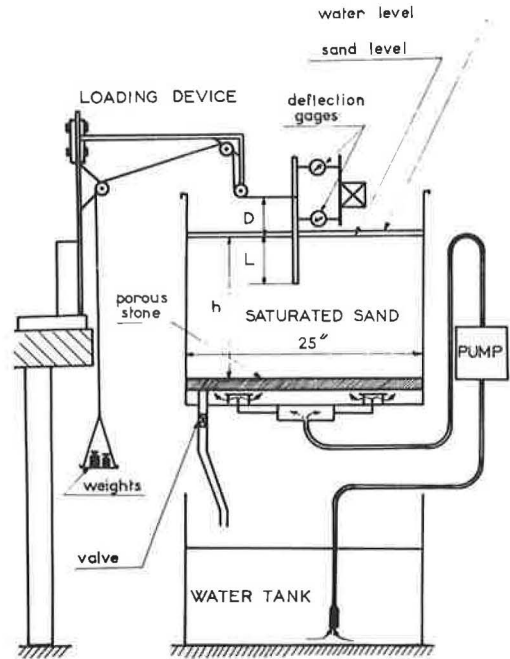
Figure 4. Schematic diagram of experimental apparatus.

EXPERIMENTAL RESULTS

The schedule of tests conducted is given in Table 3. Results of tests are shown in Figures 5 through 9 in terms of the parameters of Eq. 7; that is, the moment-strength ratio is plotted as a function of the deflection ratio X/C for various values of D/L for each particular value of C/L. Each curve represents an average of a number of tests. The experimental scatter about any single curve was quite small.

By using normalization functions for C/L and D/L, it was possible to normalize the response of Figures 5 through 9 to the particular response curve for C/L = 1.2 and D/L = 0.2, i.e., by first normalizing the various response curves for D/L to the D/L = 0.2 curve for each value of C/L by an appropriate function of D/L and then by collapsing the resulting curves which are only a function of C/L onto the C/L = 1.2 curve by another appropriate function. These normalization functions were determined to be a third-order and a second-order equation for D/L and C/L, respectively. Thus, the response can be written as:

$$\frac{M}{\gamma_d C^2 L^2 (1 + 2D_r)} = K_C K_D V(1.2 - 0.2) \tag{8}$$

where
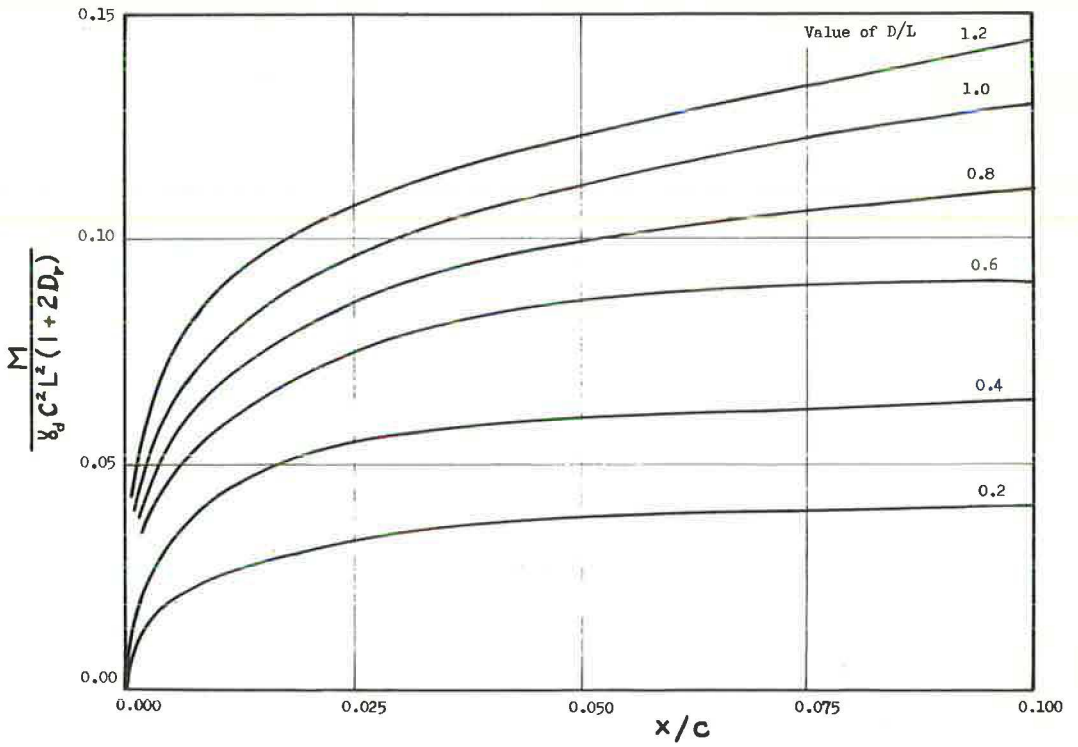
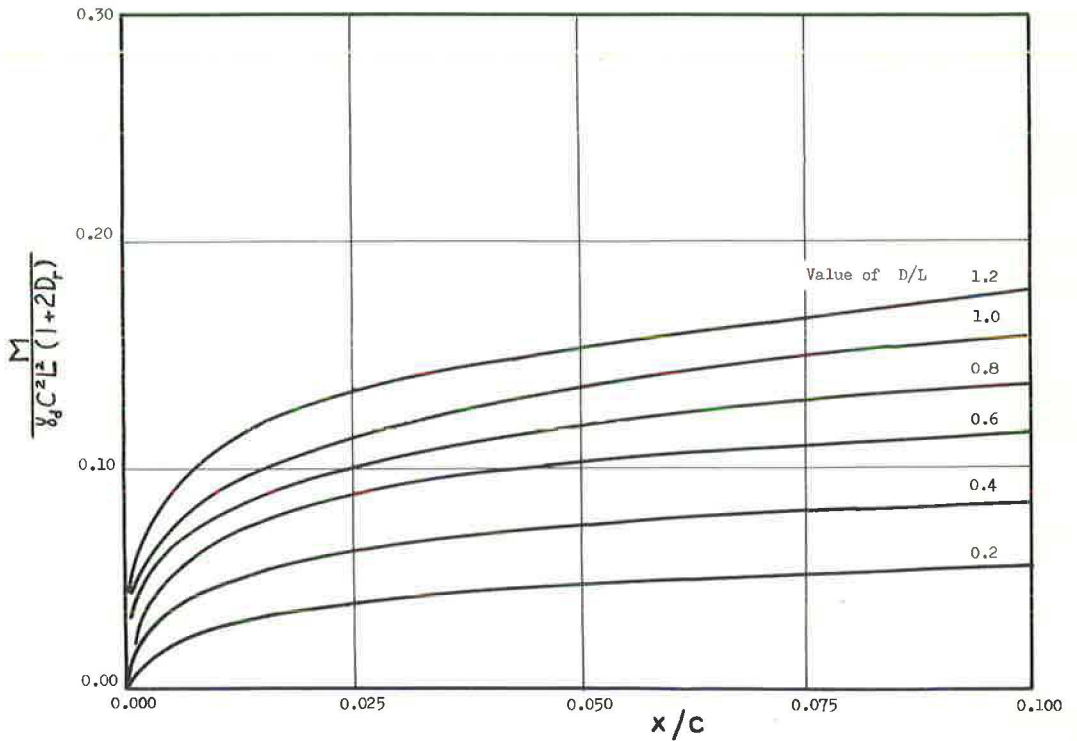Figure 5. Moment-strength parameter vs X/C for various values of D/L; C/L = 1.2.

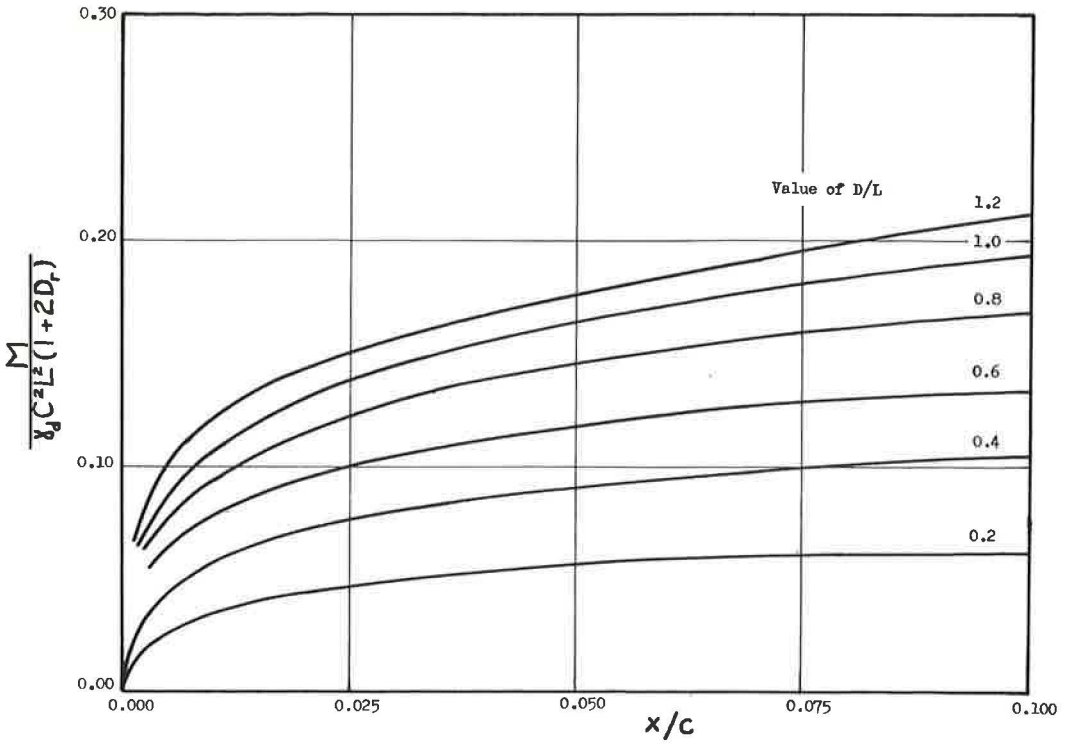Figure 6. Moment-strength parameter vs X/C for various values of D/L; C/L = 1.0.

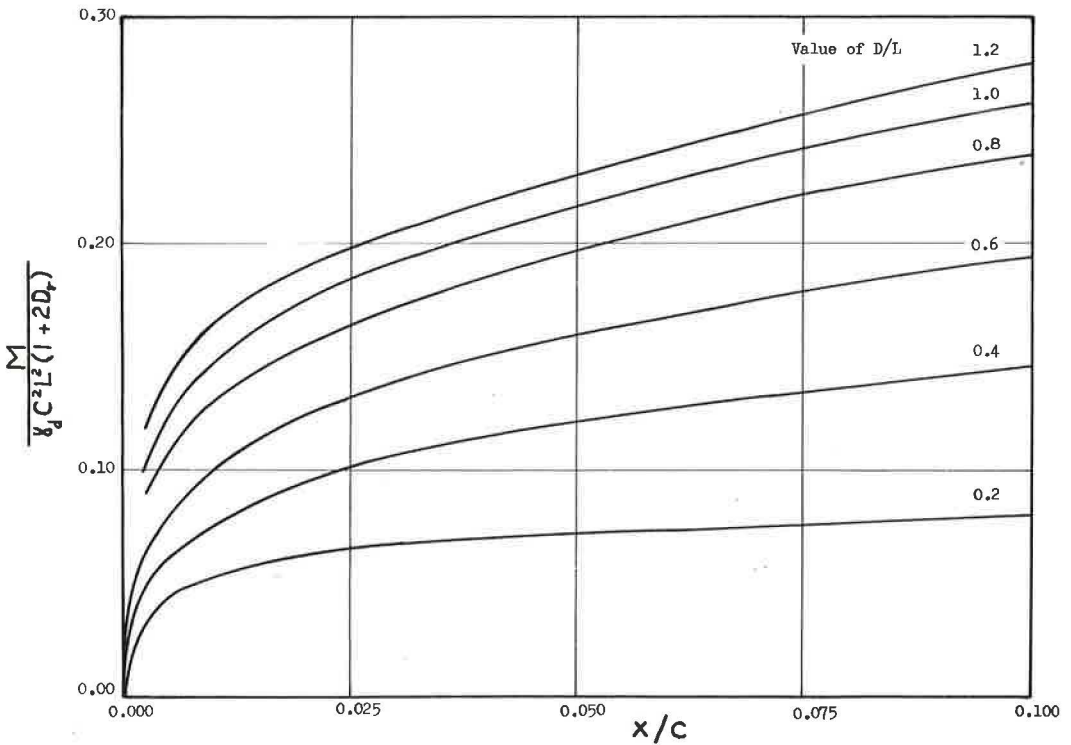Figure 7. Moment-strength parameter vs X/C for various values of D/L; C/L = 0.8.

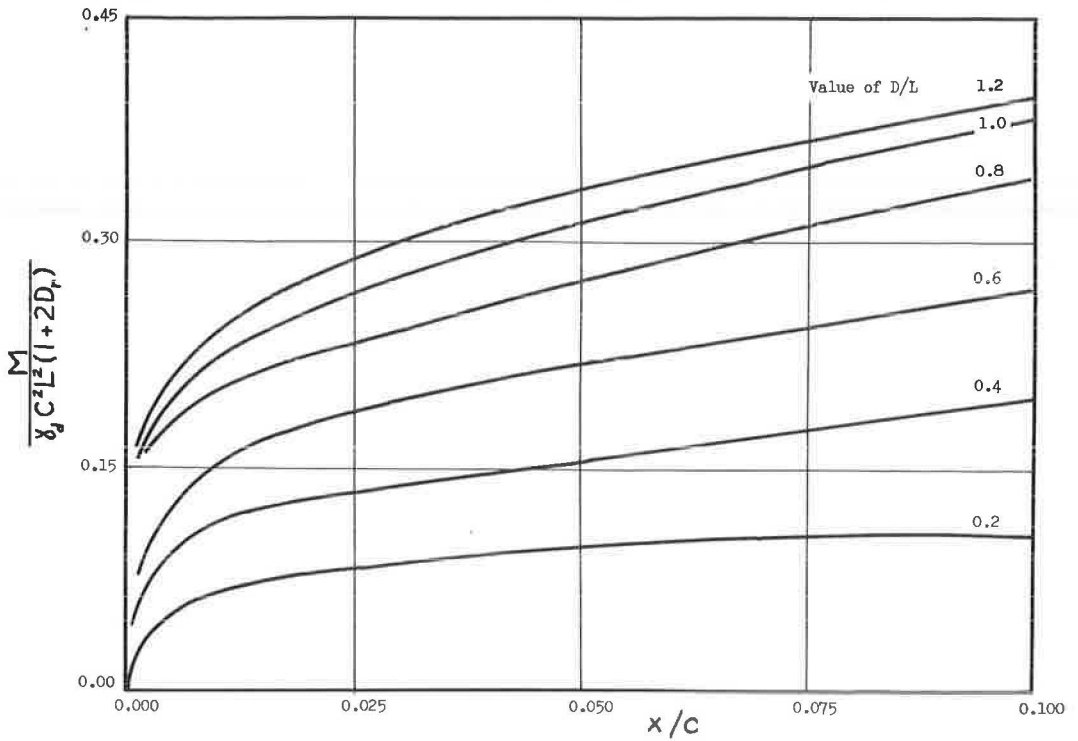Figure 8. Moment-strength parameter vs X/C for various values of D/L; C/L = 0.6.

Figure 9. Moment-strength parameter vs X/C for various values of D/L; C/L = 0.4.

$$K_D = A\left(\frac{D}{L}\right)^3 + B\left(\frac{D}{L}\right)^2 + E\left(\frac{D}{L}\right) + F, \tag{9}$$

$$K_C = G\left(\frac{C}{L}\right)^2 + H\left(\frac{C}{L}\right) + J, \text{ and} \tag{10}$$

$V_{(1.2\ -\ 0.2)}$ = curve of moment-strength parameter vs X/C for C/L = 1.2 and D/L = 0.2.

For the particular sand tested, the numerical coefficients in Eqs. 9 and 10 are A = -0.563, B = 0.194, E = 3.087, F = 0.380, G = 2.476, H = -6.209, and J = 4.887.

If the curve of the moment-strength ratio vs the deflection ratio for C/L = 1.2 and D/L = 0.2 is plotted in terms of the transformed hyperbolic coordinates (4, 5), the response given in Figure 10 is obtained. This can be written as:

$$V_{(1.2\ -\ 0.2)} = \left[\frac{M}{\gamma_d C^2 L^2 (1 + 2 D_r)}\right]_{\substack{C/L = 1.2 \\ D/L = 0.2}} = \frac{\dfrac{X}{C}}{a + b\dfrac{X}{C}} \tag{11}$$

where a = 0.175 and b = 22.532 are the slope and intercept, respectively, of the straight line of Figure 10. Physical interpretation can be attached to the constants a and b. Differentiation of Eq. 11 with respect to X/C and evaluation of the derivative at X/C = 0 gives:

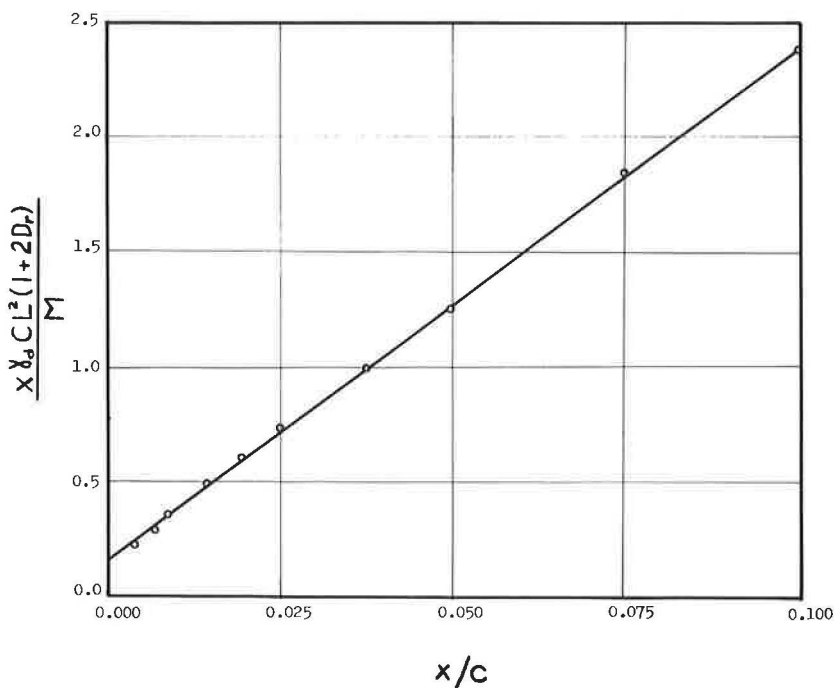Figure 10. Transformed hyperbolic representation of moment-strength ratio vs X/C; C/L = 1.2; D/L = 0.2.

$$\left[\frac{dV_{(1.2\ -\ 0.2)}}{d\dfrac{X}{C}}\right]_{\frac{X}{C}\ =\ 0} = \frac{1}{a} \tag{12}$$

Thus, the parameter $1/a$ represents a measure of the initial tangent modulus of the moment-strength ratio vs deflection ratio relation. The mathematical limit of Eq. 11 as the deflection parameter becomes excessive gives the theoretical ultimate value of the moment-strength ratio as $1/b$:

$$\left[V_{(1.2\ -\ 0.2)}\right]_{ult} = \operatorname*{Lim}_{\frac{X}{C}\ \to\ \infty} V_{(1.2\ -\ 0.2)} = \frac{1}{b} \tag{13}$$

Thus, a measure of the initial tangent modulus of the deflection ratio vs moment-strength ratio obtained from Eq. 8 is $K_C K_D/a$, and the theoretical ultimate value of the moment-strength ratio can be written:

$$\left[\frac{M}{\gamma_d C^2 L^2 (1\ +\ 2\,D_r)}\right]_{ult} = \frac{K_C K_D}{b} \tag{14}$$

The results obtained in this study and expressed in the form of Eqs. 8 through 11 agree well with the results reported by Shilts, Graves, and Driscoll (6) for both full-scale posts and large-scale model poles embedded in sand, and with the results reported

by Kondner and Cunningham (3) on small-scale model tests in dry sand. It is felt that the forms of these equations have some general applicability, but the particular values of the numerical coefficients given in this paper are limited to the present investigation. In addition, the reliability of these equations is felt to be better for the larger values of X/C.

The degree of saturation is an extremely important aspect to take into consideration when the magnitude of the numerical coefficients are obtained and utilized. Several experiments conducted by the authors in wet but not saturated sand showed that the force required for failure of a given pole at given values of C/L and D/L could be as much as 5 times larger under these conditions than under the condition of saturation used in this study. However, since a saturated situation is the most critical case and there is always the possibility of a partially saturated system becoming inundated, consideration of a sand-pole system should be conservative; hence, the saturated case is used.

SUMMARY OF METHOD

To use the method presented in this paper for a particular pole-soil system, the values of the numerical coefficients must be obtained from field tests.

Determination of a and b of Eq. 11

The parameters a and b are, respectively, the intercept and the slope obtained from a straight-line fit of a plot of $X_{\gamma d} C L^2 (1 + 2 D_r)/M$ vs X/C for a pole test with C/L = 1.2 and D/L = 0.2. Theoretically, only one test would be needed to determine the constants a and b; however, experimental error in conducting these tests indicates that a number of tests would be preferable to a single test.

Determination of A, B, E, and F

In addition to the test to obtain a and b (C/L = 1.2 and D/L = 0.2), three additional tests must be performed, e.g., C/L = 1.2 for D/L = 0.4, 0.8 and 1.2. Theoretically, these four tests will permit the calculation of the four constants A, B, E, and F. However, because of experimental error, a number of such tests would be desirable. By plotting the value of K_D of Eq. 9 as a function of D/L, intermediate values could be easily obtained.

Determination of G, H, and J

In addition to the test for C/L = 1.2 at D/L = 0.2, tests are needed for values of C/L = 0.4 and 0.8 at D/L = 0.2. These three tests can be used to determine the constants G, H, and J. Intermediate values could be obtained easily from a plot of K_C of Eq. 10 as a function of C/L.

It would be advisable to repeat each of these tests several times and to use the average curve.

CONCLUSIONS

1. The functional relationship given by Eq. 6 has been developed by the methods of dimensional analysis to describe the response of a rigid vertical pole partially embedded in sand and subjected to a horizontal load applied above the groundline. The various quantities of Eq. 6 are defined in Table 1.

2. Eqs. 8 through 11 represent the explicit form of the functional relationship as determined by small-scale model tests for circular poles embedded in a particular sand with $0.2 \leq D/L \leq 1.2$ and $0.4 \leq C/L \leq 1.2$. The form of these equations may be of considerable use in the study of prototype pole-soil systems. The values of the numerical coefficients in these equations are functions of the particular pole-soil systems and should be determined from field tests.

3. The theoretical ultimate value of the moment-strength ratio can be represented by Eq. 14 and the initial tangent modulus of the moment-strength ratio vs deflection parameter relation can be measured by $K_C K_D/a$.

Small-Scale Footing Studies on Sand and Clay

L. J. GOODMAN, Professor of Civil Engineering, Syracuse University; and
E. HEGEDUS and P. W. HALEY, Research Engineers, Land Locomotion Laboratory,
U. S. Army Tank-Automotive Center, Warren, Michigan

ABRIDGMENT

•SMALL-SCALE footings having circular, rectangular and square contact areas were
subjected to a constant rate of penetration ranging from 0.2 to 1,750 in./min. Pres-
sure sinkage relationships were obtained for footing penetrations up to 4 in. to deter-
mine the influence of sinkage rate and footing geometry on load sinkage characteristics
of soils. Particular attention was given to the initial portions of the load sinkage curves
to determine typical failure patterns and bearing capacities.

Test soils consisted of a wet Ottawa sand, prepared by flooding the entire soil bin
and then compacting by quick drainage, and a remolded Boston blue clay. Control
parameters measured in each test condition were moisture content and density. Opera-
tional principles of the loading device are shown in Figure 1.

With increased rates of penetration, the resistance of both soils to penetration in-
creased. Typical pressure sinkage curves with rates of sinkage as a parameter are
shown in Figures 2 and 3 for sand and
clay, respectively. In sand, 60 in./min
was observed as the critical deformation
rate at which the mode of failure changed.
For sinkage rates slower than 60 in./min,
local shear failure was predominant, and
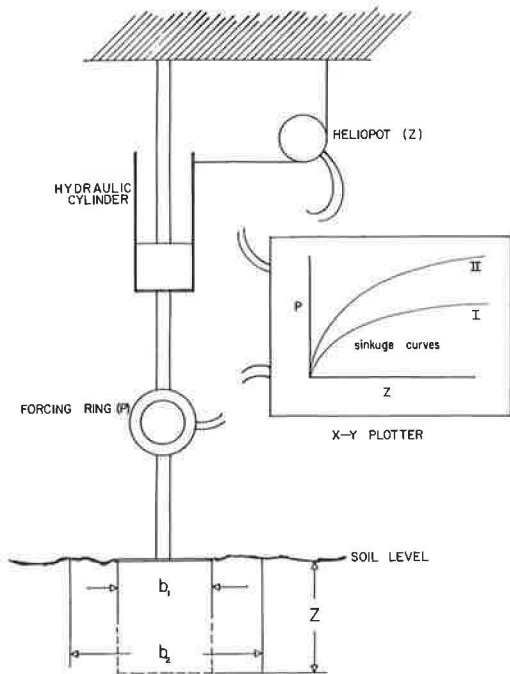for higher sinkage general shear failure
was predominant. These conclusions
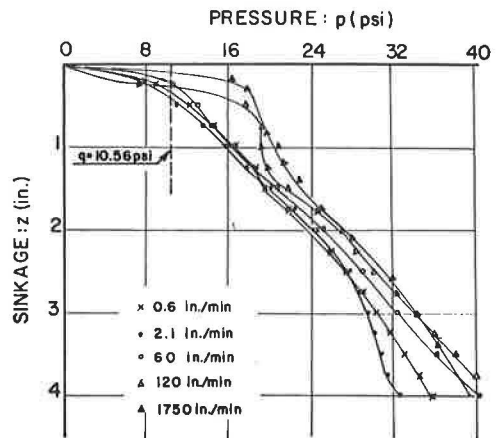

Figure 1. Load sinkage bevameter diagram.

Figure 2. Pressure-sinkage curves for $2\frac{1}{2}$-
in. diameter footing in sand.

ACKNOWLEDGEMENT

REFERENCES

1. Kerisel, J. La Force Portante des Pieux. Ann. des Ponts et Chaussees, 1939.
2. Kondner, R. L., and Green, G. E. Lateral Stability of Rigid Poles Subjected to a Ground-Line Thrust. Highway Research Board Bull. 342, pp. 124-151, 1962.
3. Kondner, R. L., and Cunningham, J. A. Lateral Stability of Rigid Poles Partially Embedded in Sand. Highway Research Record No. 39, pp. 49-67, 1963.
4. Kondner R. L. Hyperbolic Stress-Strain Response: Cohesive Soils. Jour. Soil Mech. and Found. Div., ASCE, Vol. 89, SM 1, pp. 115-143, 1963.
5. Kondner, R. L., and Zelasko, J. S. A Hyperbolic Stress-Strain Formulation for Sand. Proc. 2nd Pan-American Conf. on Soil Mech. and Found. Eng., Brazil, pp. 289-324, 1963.
6. Shilts, W. L., Graves, L. D., and Driscoll, G. G. A Report of Field and Laboratory Tests on the Stability of Posts Against Lateral Loads. 2nd Int. Conf. of Soil Mech. and Found. Eng., Vol. 5, pp. 107-122, 1948.
7. Davisson, M. T., and Prakash, S. A Review of Soil-Pole Behavior. Highway Research Record No. 39, pp. 25-48, 1963.
8. Broms, B. B. Lateral Resistance of Piles in Cohesionless Soils. Jour. Soil Mech. and Found. Div., ASCE, Vol. 90, SM 3, pp. 123-156, 1964.
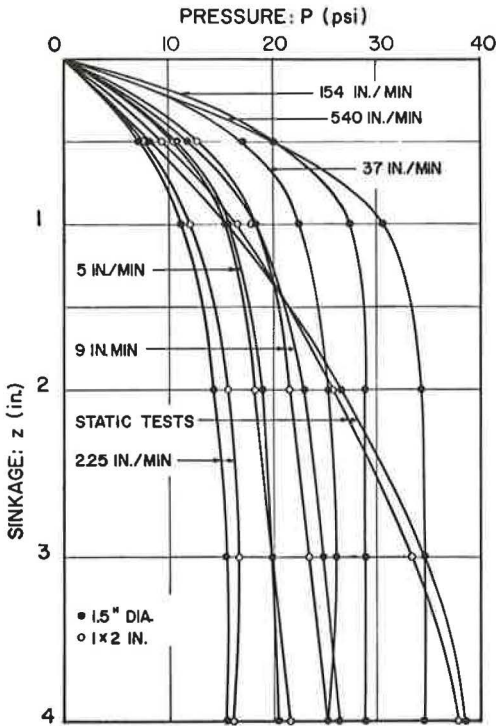
Figure 3. Pressure-sinkage curves at seven rates of loading for remolded clay.
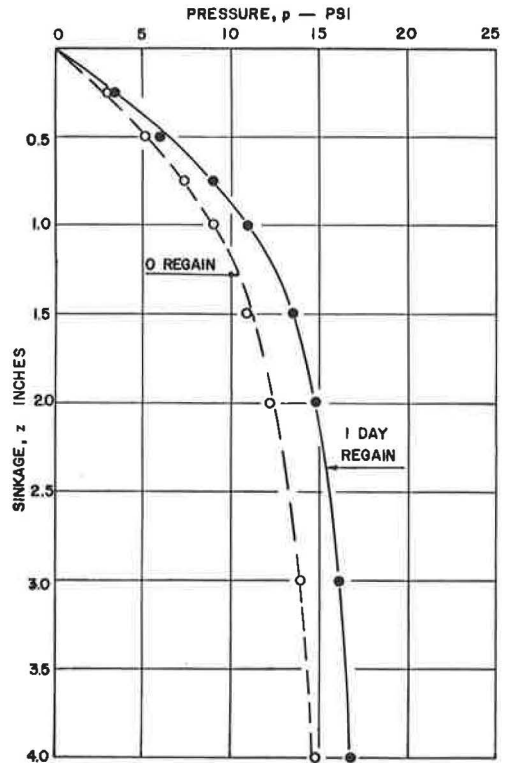

Figure 4. Thixotropic regain of resistance to footing sinkage in remolded clay.

were true for all except for the $\frac{3}{4}$- by 4-in. footings which failed due to general shear failure occurring at all sinkage rates tested. Local shear failure pattern was indicated from the remolded clay with all the small-scale footings investigated under the various penetration rates.

The increase in strength with increased rates of penetration was attributed to inertia effects in both soils and also to the change in the mode of failure in sand and to the plastic resistance in clay. The ultimate bearing capacity of clay occurred at excessive footing sinkages; therefore, it became apparent that the safe soil pressure of a remolded soft clay has to be based on settlement considerations.

In sand, the measured bearing capacity values at sinkage rates higher than 120 in./min were found to be twice as high as one would expect from static tests. The low deformation rate tests obtained in sand were in reasonable agreement with Terzaghi's bearing capacity theory; however, no agreement between theory and experiments were noted in the clay.

The significance of thixotropic regain characteristics of Boston blue clay after remolding is demonstrated in Figure 4, which shows the influence of a regain period of 1 day in connection with resistance to sinkage of a 3.5-in. diameter footing. The results would tend to confirm the influence of thixotropic regain characteristics on the strength of the clay as obtained from the static loading test. The loading period involved a time element of 2 weeks, which has been found to be very significant relative to an increase in resistance to sinkage.

Mobility Soil Mechanics

L. J. GOODMAN, Professor of Civil Engineering, Syracuse University; and
R. A. LISTON, Land Locomotion Laboratory, U. S. Army Tank-Automotive Center,
Warren, Michigan

ABRIDGMENT

•THE DEVELOPMENT of land locomotion mechanics has required a departure from
soil mechanics as applied to highway design. When dealing with off-road vehicle de-
sign, the engineer is faced with extremely large shear and sinkage deformations that
extend well beyond the elastic or linear stress-strain range of soil.

Equations describing soil pressure-sinkage relationships and shear strength-defor-
mation are presented. The pressure-sinkage equation is of the form:

$$p = kz^n \tag{1}$$

where

p = pressure,
k = proportionality constant containing both soil and load constants,
z = sinkage, and
n = a dimensionless exponent.

The shear strength-deformation equation is of the form:

$$S_z \, (c + p \tan \phi) \, (1 - e^{-j/k}) \tag{2}$$

where

S = unit shear strength,
c = cohesion as measured by an annular shear device,
ϕ = angle of internal friction as measured by an annular shear device,
j = any shear deformation, and
k = the modulus of deformation (tangent modulus).

The motion resistance of a vehicle is proportional to the sinkage and the tractive
effort is proportional to the shear strength. The development of equations describing
these proportions permits the prediction of vehicle performance.

The problem of the highway engineer is quite different from the off-road vehicle de-
sign engineer in that the former is concerned with soil loading situations producing very
small deformations. It is concluded, however, that despite the difference in soil prob-
lems, the civil engineer may find the approach taken by mobility soil mechanics use-
ful when dealing with slope stability, piles, and other problems which may result in
large deformations.